The Institute for Solid State Physics
The University of Tokyo

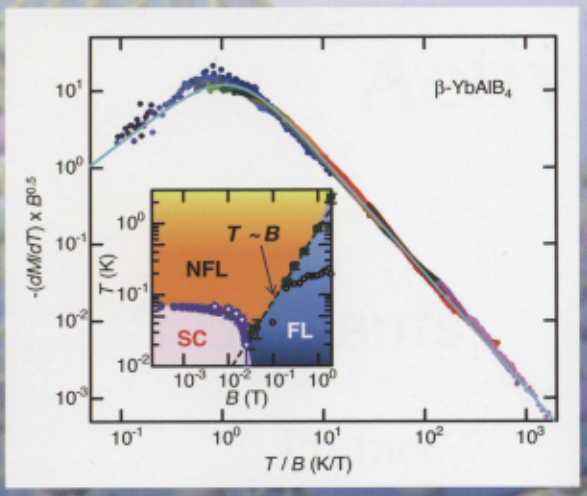

Activity Report 2010

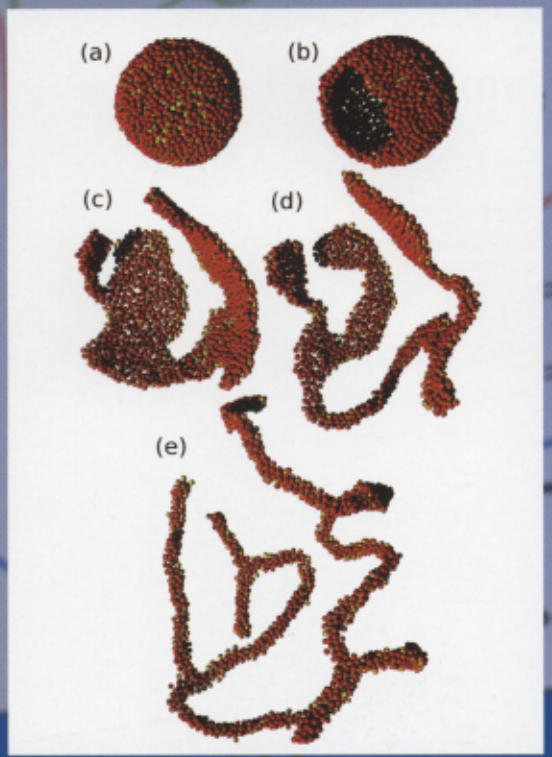

ISSP

Activity Report 2010

Contents

Preface

This booklet constitutes the annual Activity Report of the Institute for Solid State Physics (ISSP), the University of Tokyo for the academic year 2010.

ISSP was established in 1957 as a joint-use central research institution in the field of basic materials science. After its 40 years of operation at the Roppongi campus, ISSP relocated itself to a new campus in Kashiwa city and started afresh in April 2000. The relocation was a good occasion for renovation and upgrading of the research facilities and infrastructures. This Activity Report as well as those in previous years presents some of the research accomplishments of ISSP during the first 10 years in Kashiwa.

In recent years, research activities using large facilities have gained importance in materials science which is traditionally thought to belong to the so-called small science category. ISSP is in charge of operating some of those large facilities which are difficult to be maintained by ordinary university faculties. Here we briefly report the status quo of those undertakings. The Materials Science Beam-Line completed in October 2009 at the BL07LSU site of the SPring-8 Facility in Harima is now in full operation to pour out high quality data. The High-Resolution Chopper Spectrometer for neutron scattering experiments was constructed at the BL12 of J-PARC/MLF in collaboration with KEK. The non-destructive long-pulse magnet project is vigorously pursued with a dc generator with flywheel in the International Megagauss Science Laboratory. As for the destructive ultrahigh magnetic field project by the electromagnetic compression method, upgrading of the capacitance bank system has been granted recently by the MEXT. As for the Next-Generation Supercomputer Project, ISSP has been selected as the representative institute to lead the research in the Strategic Field 2 “New Materials and Energy Creation”.

Such was the state of affairs at the turn of the academic year 2010 to 2011. It was overwhelmed by a massive earthquake and tsunami that hit the Pacific coast side of the Northeastern Region of Japan on March 11. We should like to express our condolences to the victims of this unprecedented disaster. We should also like to appreciate hearty inquiries concerning our safety and facility damage sent by many colleagues around the world. Fortunately, there were no casualties incurred among the members of ISSP. The damage to the facilities and equipments is minimal in Kashiwa Campus. On the other hand, the damage is rather extensive at the neutron facilities in Tokai (J-PARC and JRR-3) and the synchrotron radiation facility (Photon Factory) in Tsukuba. Nevertheless, we started the restoration process of those facilities in collaboration with the related organizations. Even though it surely is a difficult situation, we are regaining our composure from this unprecedented disaster. We shall make every effort to move forward and get back to full operation as soon as possible and shall show ourselves more powerful than ever.

May, 2011

Yasuhiro Iye
Director
Institute for Solid State Physics
The University of Tokyo

Anomalously Low Compressibility of Silica Glass in Helium

Yagi Group

SiO_2 is an archetypal oxide as well as an archetypal glass-forming material, and is also the most abundant component of terrestrial rocks. Therefore, SiO_2 glass has been studied extensively in various fields of physical sciences. SiO_2 glass is compressible among silicates (or oxides) because it has a structure with a significant amount of interstitial voids. Helium is monatomic and the smallest molecule, and therefore is used as a light inert gas. It is also widely used as the most ideal pressure medium in high-pressure experiments. Its isotopic ratio is useful as a tracer of the Earth's evolution. Here we report anomalous behavior of SiO_2 glass in helium under high pressure [1].

The volume change (V/V_0) was determined by measuring the change in the size of the bulk sample compressed in a diamond-anvil cell. As shown in Fig. 1, it was found that SiO_2 glass is much less compressible than normal when compressed in a helium medium, suggesting that the voids in SiO_2 glass are prevented from contracting because a large amount of helium penetrates into these voids. X-ray diffraction measurements show that the pressure-induced shift of the position of the first sharp diffraction peak (FSDP) in

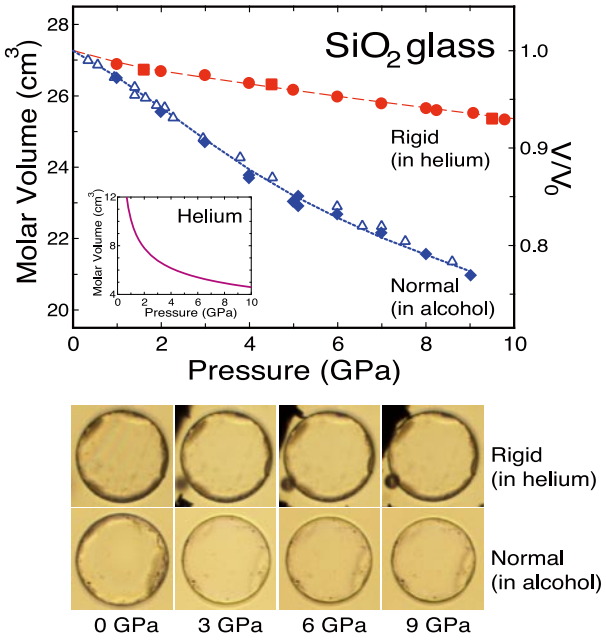

Fig. 1. Pressure dependence of the volume of SiO_2 glass. The red and blue filled symbols represent our data in helium and methanol-ethanol, respectively. The blue open symbols and dotted line represent the data in methanol-ethanol in the literature. The photographs compare the change in the size of the bulk sample compressed in the two pressure mediums. While the samples are almost the same size, about 80 μm in diameter at 0 GPa, the sample in methanol-ethanol is obviously smaller than that in helium at 9 GPa.

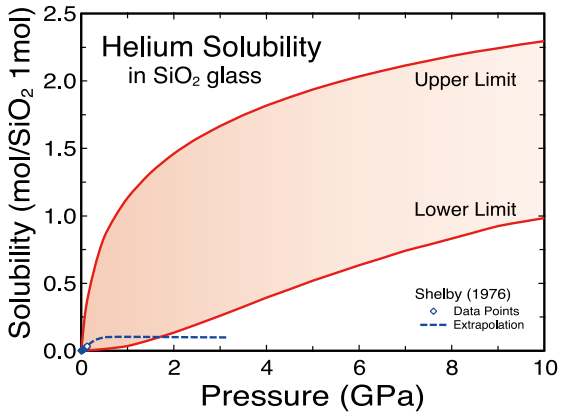

Fig. 2. Estimated lower and upper limits on helium solubility in SiO_2 glass. An extrapolation of the low-pressure data based on a statistical thermodynamical model (blue broken line) cannot explain the volume changes measured at higher pressures.

helium is much smaller than that in normal cases. Raman scattering measurements also show that spectra in helium are significantly different from those in normal cases. These results are consistent with the small change in volume.

The helium solubility in SiO_2 glass, estimated from the volumes of SiO_2 glass and helium, is shown in Fig. 2. The estimated solubility is very high and is between 1.0 and 2.3 mol per mole of SiO_2 glass at 10 GPa. The maximum solubility of helium in SiO_2 glass has been estimated to be 0.1 mol per mole of SiO_2 glass, based on measurements up to about 0.1 GPa. Moreover, gas solubilities have been expected to decrease drastically at higher pressures due to compaction of voids. However, these well-accepted models cannot explain our volume measurements shown in Fig. 1.

Our results may affect discussions on the Earth's evolution as well as interpretations of various high-pressure experiments, and also lead to the creation of new materials. The fact that helium solubility in SiO_2 glass at high pressures is completely different from the estimation based on the data at low pressures may suggest the necessity of reconsidering conventional models on degassing from the mantle and other relevant events in the Earth's history. Our results also suggest the possibility that a helium pressure medium may affect the compression behavior of materials with voids. When helium atoms occupy these voids, the materials are compressed not only from outside but also from inside. This is very different from normal compression. Therefore, in addition to the effects on compressibilities, applying pressure in helium could be an interesting way to synthesize novel phases.

Reference

[1] T. Sato, N. Funamori, and T. Yagi, Nature Communications **2**, 345 (2011)

Authors
T. Yagi, T. Sato, and N. Funamori[a]
[a]Department of Earth and Planetary Science, University of Tokyo

Evidence of a Field-Induced Ordering in the Heavy Fermion Compound $YbCo_2Zn_{20}$

Sakakibara Group

Recently, the cubic heavy-fermion compound $YbCo_2Zn_{20}$ has attracted much interest because of its gigantic electronic-specific-heat coefficient γ = 7900 mJ $mol^{-1}K^{-2}$ [1]. Several experiments suggest that this heavy-fermion compound is close to a quantum critical point. For instance, a metamagnetic peak has been observed in the field-dependent AC susceptibility at a very low field of 0.5 T at low temperatures below 0.2 K [2]. In particular, a magnetic phase has been reported to appear under a pressure of 1 GPa [3]. In order to shed more light on the critical behavior of $YbCo_2Zn_{20}$, we have measured the DC magnetization M (H, T) of a single-crystal sample in magnetic fields up to 14.5 T at very low temperatures down to 0.08 K [4].

Figure 1 shows the magnetization $M(H)$ for $H \parallel [111]$ obtained at the base temperature. Although not shown, $M(H)$ shows a strong cubic anisotropy in fields above 2 T with [111] being the hard axis. In addition to the 0.5 T transition described above, we found a metamagnetic transition at 6 T only for $H \parallel [111]$ as shown in Fig. 1. Moreover, a prominent kink is found to appear in $M(T)$ in the temperature range below 0.6 K at fields above 6 T. These results strongly suggest that an ordered phase exists for $H \parallel [111]$ in the region $\mu_0 H \geq 6$ T and $T \leq 0.6$ K. As far as we know, $YbCo_2Zn_{20}$ is the first Yb-based compound in which a field-induced ordering has been observed. The obtained H-T phase diagram is shown in Fig. 2, where FIOP denotes the field-induced ordered phase. We also found that a broad peak shows up in $M(T)$ at fields above 3 T, whose peak position is indicated by $T_{M\,max}$ in Fig. 2. These results are best explained by a level crossing of the low-lying crystalline-electric-field state with the ground state. The results further suggest that a strong magnetic field drives the Yb ions in this compound toward a trivalent state.

References

[1] M. S. Torikachvili *et al.*, Proc. Natl. Acad. Sci. U. S. A. **104**, 9960 (2007).
[2] M. Ohya *et al.*, J. Phys. Soc. Jpn. **79**, 083601 (2010).
[3] Y. Saiga *et al.*, J. Phys. Soc. Jpn. **77**, 053710 (2008).
[4] Y. Shimura, T. Sakakibara, S. Yoshiuchi, F. Honda, R. Settai, and Y. Onuki, J. Phys. Soc. Jpn. (to be published).

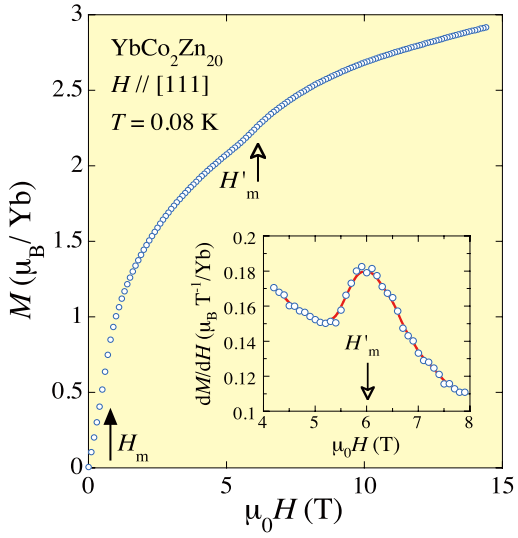

Fig. 1. Field dependence of the magnetization M(H) of $YbCo_2Zn_{20}$ for H ∥ [111] measured at 0.08 K. A metamagnetic transition is found at H'_m=6 T. The inset shows dM/dH near H'_m.

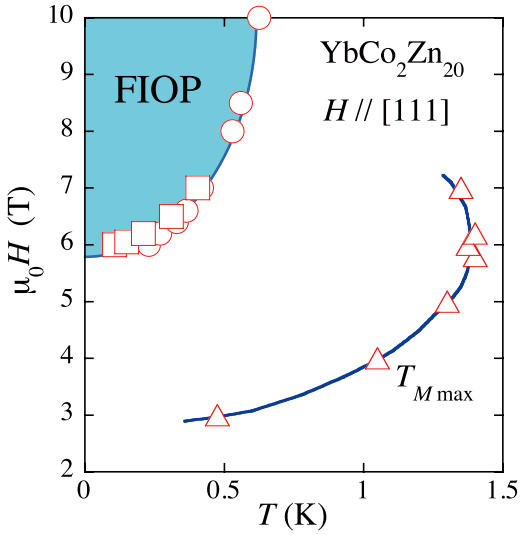

Fig. 2. H-T phase diagram of $YbCo_2Zn_{20}$ for $H \parallel [111]$. FIOP indicates the field-induced ordered phase. $T_{M\,max}$ denotes the temperature where the temperature variation of the magnetization $M(T)$ takes a local maximum.

Authors

Y. Shimura, T. Sakakibara, S. Yoshiuchi[a], F. Honda[a], R. Settai[a], and Y. Onuki[a]

[a]Osaka University

Synergy between Spin Crossover and Dielectric Relaxation in the Fe(III) Complex

Mori Group

The synergy between magnetism of spin crossover (SCO) phenomena and other electronic properties such as conductivity, magnetism, and optics, can provide an opportunity to control their multiple properties by external stimuli such as temperature, pressure, magnetic field, and light. Previously, SCO molecular conductors have been developed, [1] in which conductivity modulation can be achieved by using a type of chemical pressure effect, namely a remarkable structural change of SCO cations accompanying a spin conversion. In this study, we report the preparation, crystal structures, physical properties of the first Fe(III) SCO complexes with an acidic HSO_4 anion, $[Fe^{III}(qsal)_2](HSO_4)\cdot CH_3OH$ **1** and $[Fe^{III}(qsal)_2](HSO_4)\cdot 0.5CH_3OH$ **2** [qsalH = *N*-(8-quinolyl)salicylaldimine], and the synergic behavior between SCO conversion and dielectric relaxation in **2**.

The iron(III) complex containing an HSO_4 anion **1** was prepared as small black rhombic crystals by slow diffusion methods using an H-type glass cell between $[Fe(qsal)_2]Cl\cdot 1.5H_2O$ and n-$Bu_4N\cdot HSO_4$ in methanol at room temperature. The aged complex **2** was unexpectedly obtained by storing the crystals of **1** for 3 months at room temperature. The crystal structures of **1** and **2** are isostructural. The difference of the cell volumes between **1** and **2** is *ca.* 40 $Å^3$ of one methanol molecule. As shown in Figure 1, $Fe(qsal)_2$ molecules construct a π–π interaction framework affording a one-dimensional channel along the *a* axis, in which HSO_4 anion and methanol molecules exist. In the one-dimensional channel, HSO_4 anions form a dimer via strong hydrogen bonds for **1** and **2**. Two methanol molecules hang on a HSO_4 dimer through hydrogen bonds for **1**, forming a symmetrical hydrogen-bonded cluster, whereas only the carbon and

oxygen atoms with 50% occupancy are found for **2** (Fig. 1).

The temperature dependence of magnetic susceptibility for **1** is shown in Figure 2(a). On lowering the temperature, the $\chi_M T$ value (3.97 cm^3 K mol^{-1}) of **1** at 300 K in the HS state decreased abruptly at 160 K ($T_{1/2}\downarrow$ = 157 K) to transform to the LS state (0.57 cm^3 K mol^{-1}) below 120 K. On heating, the spin conversion from the LS to HS states occurred at around 150 K and the $\chi_M T$ value recovered the original HS value at 170 K ($T_{1/2}\uparrow$ = 161 K). The temperature dependence of Mössbauer spectra for **1** also indicates that the high temperature (HT) and the low temperature (LT) phases are completely in the HS and LS states, respectively. Interestingly, the three-month-aged sample **2** demonstrated a completely different magnetic behavior [Figure 2(b)]. On lowering the temperature, the $\chi_M T$ value decreased gradually ($T_{1/2}\downarrow$ = 231 K). The shift of the transition temperatures for **2** can be explained in terms of a chemical pressure effect induced by the lack of a methanol molecule. In the heating process, the $\chi_M T$ value recovered the HS value at 300 K ($T_{1/2}\uparrow$ = 284 K), but the recovery process depends on sample treatments. Note that after several successive cooling and heating cycles the spin transition temperature for **2** shifted to the same temperature for **1**. These observations suggest that the aged sample **2** has the metastable state closely related to **1**.

In order to clarify the dielectric properties for **1** and **2**, the temperature dependence of permittivity was measured on a compressed pellet with quasi 4-probe method by an Agilent 4294 precision impedance analyzer. The thermal hysteresis loop of ε' for **1** was observed in the similar temperature range to that of magnetic susceptibilities. The dielectric constants ε' for **1** are small and almost frequency independent [Figure 2(c)]. On the other hand, the temperature dependence of dielectric constants ε' for **2** revealed that the dielectric constants are relatively large and frequency-dependent [Figure 2(d)]. The imaginary part of the dielectric constants ε" also showed frequency-dependent peaks upon

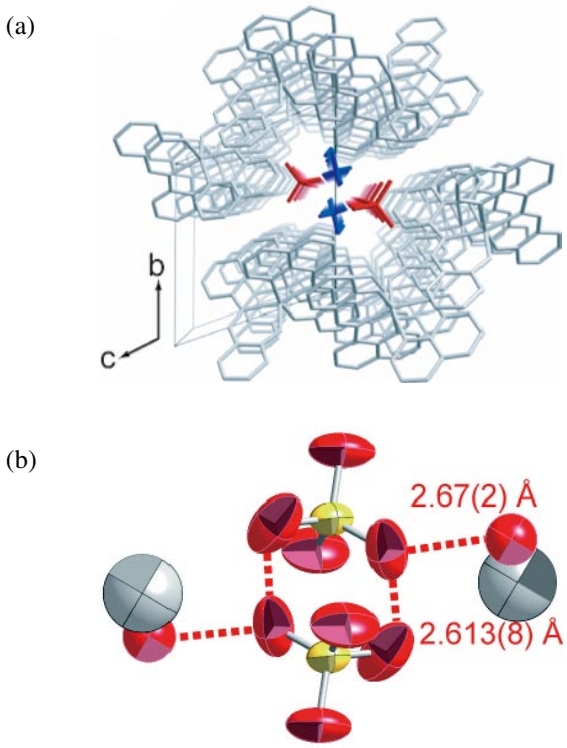

Fig. 1. Perspective view of a one-dimensional channel along the *a* axis and the anion-solvent cluster of $[(HSO_4)\cdot 0.5CH_3OH]_2$ for the Fe(III) spin crossover complexes $[Fe^{III}(qsal)_2](HSO_4)\cdot 0.5CH_3OH]$ **2** [qsalH = *N*-(8-quinolyl)salicylaldimine].

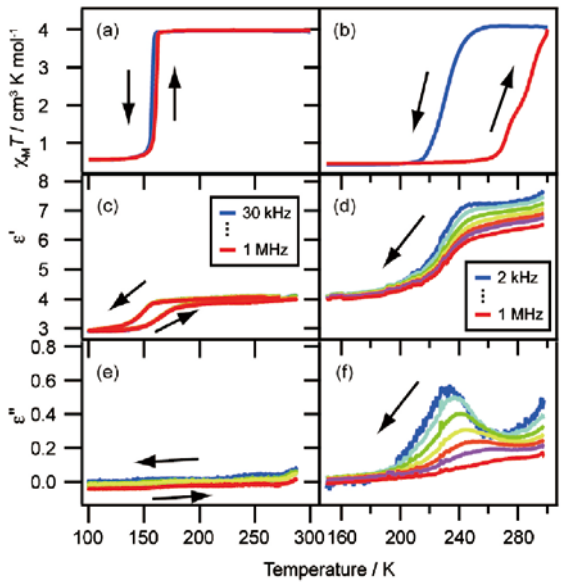

Fig. 2. The temperature dependence of magnetic and dielectric properties for $[Fe^{III}(qsal)_2](HSO_4)\cdot CH_3OH]$ **1** and $[Fe^{III}(qsal)_2](HSO_4)\cdot 0.5 CH_3OH]$ **2**. (a) and (b) $\chi_M T$ vs. *T*, magnetic field: 0.5 T, scan speed: 1 K min^{-1}, (c) and (d) ε' vs. *T*, (e) and (f) ε" vs. *T* for **1** and **2**, respectively. The synergy of spin crossover and frequency-dependent dielectric response has been observed for **2** due to the dipole of the cluster $[(HSO_4)\cdot 0.5CH_3OH]_2$.

the dielectric conversion, indicating that dielectric relaxation based on the motion of dipole moments occurred [Figure 2(f)]. The different dielectric behaviors between the isostructural compounds **1** and **2** clearly suggest that a correlation between disordered methanol molecules and dielectric relaxation.

The crystal structures of the LT and HT phases for **1** indicate that the disorder-order motion of the symmetrical cluster of HSO_4 anion and methanol molecules is coupled to a complete SCO transition between the HS and LS states in **1**. This motion in **1** resulted in the small frequency-independent dielectric responses. On the other hand, the unsuccessful crystal analysis using a lower crystal symmetry (*P*1) and no observation of diffuse or superlattice spots for **2** suggest that the position of a methanol molecule in **2** is completely disordered. Therefore, there is an asymmetrical hydrogen-bonded cluster composed of one methanol molecule and an HSO_4 anion dimer in the one-dimensional channel of SCO framework for **2**. The thermal ellipsoids of oxygen atoms of an HSO_4 anion in **2** are also larger than those in **1**. Hence, the dipole moments of this asymmetrical cluster can respond to electric field in the HT phase of **2**. This indicates that the dielectric relaxation coupled to the SCO conversion for **2** would originate from the motion of the asymmetric hydrogen-bonded cluster.

In summary, we successfully prepared the novel Fe(III) SCO compounds with an acidic HSO_4 anion, **1** and **2**. The compound **2** is the first SCO complex that exhibits the dielectric relaxation coupled to the SCO transition. These results open the possibility to meet molecular metal coordination compounds with *protonics* derived from inorganic solid acids.

Reference

[1] K. Takahashi, H.-B. Cui, Y. Okano, H. Kobayashi, Y. Einaga, and O. Sato, Inorg. Chem. **45**, 5739 (2006); K. Takahashi, H.-B. Cui, Y. Okano, H. Kobayashi, H. Mori, H. Tajima, Y. Einaga, and O. Sato, J. Am. Chem. Soc. **130**, 6688 (2008).

Authors
K. Takahashi, H. Mori, Y. Einaga[a], K. Yamamoto[b], K. Yakushi[b], and O. Sato[c]
[a]Keio University
[b]Institute for Molecular Science
[c]Kyushu University

Determination of Trap Density Function Based on Photo-CELIV Measurements at Low Temperatures

Tajima Group

The concept of "effective mobility" is well-established in thin-film organic semiconductors. It relates various properties of organic devices to those of inorganic devices. However, its validity has not been examined in wide temperature range. Since this concept is based on the hopping model, it should be no more valid at extremely low temperatures. Thus the following questions arises: What is the temperature range where the concept is valid? What is an appropriate model at low temperatures instead of the "effective mobility" model?

In order to answer these questions we performed the photo-CELIV (CELIV = carrier extraction by linearly increasing voltage) experiments for ITO/ PEDOT: PSS / P3HT: PCBM / Al over a wide temperature range from 210 K down to 1.6 K. Figure 1 shows the experimental scheme of photo-CELIV measurement. In this measurement, the photo carriers are generated inside a photovoltaic cell using a light pulse. After a delay time of t_d, the photogenerated carriers are extracted by linearly ramping reverse voltages. Since a sample device behaves as a capacitor for the reverse bias voltages applied, a step-like displacement current is observed for the ramping in the dark. When the light pulse is irradiated before the ramping, a CELIV signal which corresponds to an extra current due to the photogenerated carriers appears. The mobility of organic thin films can be estimated from t_{max}, the time to reach the current maximum of the CELIV signal, using the following equation [1]:

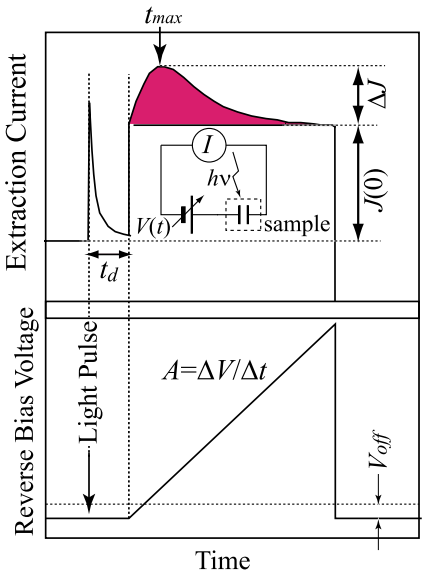

Fig. 1. Experimental scheme for the photo-CELIV measurements. The parameters t_d, A, and V_{off} denote the delay time, the rate of voltage increase, and offset reverse bias voltage, respectively. The red shaded part is the CELIV signal.

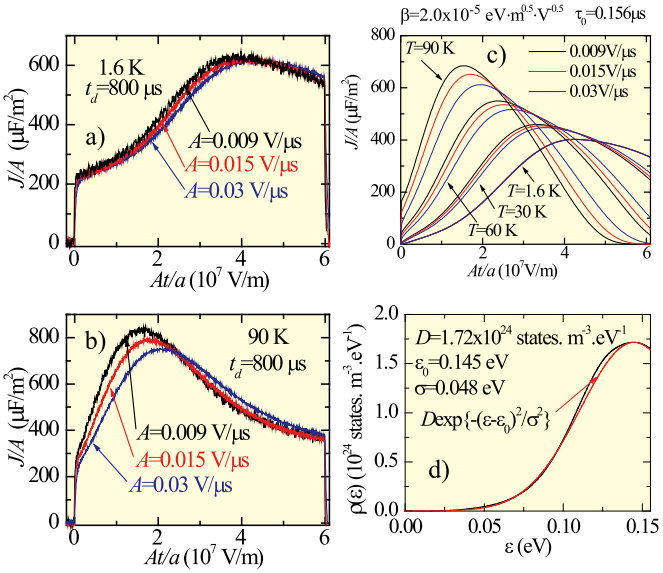

Fig. 2. (a),(b): Measured photo-CELIV signals at 1.6 and 90 K. The parameter A is the rate of voltage increase. Note that CELIV signal is almost universally scaled in this plot at 1.6 K. (c): Calculation of CELIV signal based on the "trap model". (d): Black line shows the trap-density function experimentally determined from the data of (a). The red line shows a fit of Gaussian function to the observed function.

$$\mu = \frac{2a^2}{3At_{\max}^2[1+0.36\frac{\Delta J}{J(0)}]}. \qquad (1)$$

Here a, A, and $\Delta J/J(0)$ are respectively the distance between electrodes, the rate of voltage increase, and the ratio of the current at t=0 to the maximum extraction current.

We first applied this equation and evaluated the effective mobility in wide temperature range. The equation predicts that the peak voltage of the CELIV signal is given by $V_{\max} = At_{\max} \propto \sqrt{A/\mu}$ when we evaluate $V_{\max}$ by using Eq. (1) while neglecting the term of $[1+0.36\Delta J/J(0)]$. Thus we should observe a peak shift associated with the change of A when using Eq. (1). As can be seen from Fig. 2(a, b), such a shift is observed at 90 K but is hardly observed at 1.6 K. Then we discarded this model and analyzed the CELIV data based on a "trap-limited current" model.

In this model, we assume that CELIV signal reflects charge carriers evacuating from traps under a strong electric field applied. We evaluate the decrease of activation energy under the electric field using Poole-Frenkel effect. Then we obtain

$$J/A = \frac{1}{AS}\frac{dQ}{dt} = -\int e\rho(\varepsilon)\frac{df(\varepsilon,F)}{dF}d\varepsilon \qquad (2)$$

$$X = \frac{a}{A\tau_0}\left(\frac{2F^{0.5}kT}{\beta} - \frac{2k^2T^2}{\beta^2}\right)\exp\left(\frac{-\varepsilon+\beta F^{1/2}}{kT}\right)$$

$$+\frac{a}{A\tau_0}\left(\frac{2k^2T^2}{\beta^2}\right)\exp\left(\frac{-\varepsilon}{kt}\right) \qquad (3)$$

$$f = \exp(-X) \qquad (4)$$

In the case of $T\to 0$, Eqs. (2)~(4) are reduced into

$$\frac{J}{A} = \frac{e\beta F^{-1/2}}{2}\rho\left(\beta F^{1/2}\right). \qquad (5)$$

Thus once β is determined, the trap density function is

directly evaluated from the photo CELIV signal at the lowest temperature. We estimated β by analyzing the temperature dependence of the CELIV signals using Eqs. (2)~(4).

Figure 2(c) shows the calculated CELIV signal using this model. The CELIV signal does not depend on *A* at low temperatures but depends on *A* at higher temperature. This is consistent with the observations. Moreover, considering the contribution of displacement current (approximately 230 μF· m^{-2}), the consistency between the calculated and observed CELIV signals is satisfactory.

The analysis demonstrates the validity of the "trap-limited current" model for the organic thin films at low temperatures.

References
[1] A. J. Mozer *et al.*, Phys. Rev. B **72**, 035217 (2005).
[2] H. Tajima *et al.*, J. Phys. Soc. Jpn. **80**, 063705 (2011).

Authors
H. Tajima and M. Yasui

Novel Successive Phase Transitions and Phase Diagrams of $Rb_4Mn(MoO_4)_3$: A Model Compound in Quasi-Two-Dimensional Antiferromagnet

Nakatsuji, Sakakibara, Tokunaga, and Kawashima Groups

Geometrically frustrated magnetism has been a subject of active research in condensed matter physics. Generally in physics, quantitative comparison between experiment and theory is crucial to make a firm progress of our understanding. In the field of frustrated magnetism, however, such fortuitous cases are still scarce where full or semi quantitative agreement between experiment and theory have been found, except a few examples such as spin ice [1] and the orthogonal dimer $SrCu_2(BO_4)_2$ [2].

Two-dimensional (2D) triangular antiferromagnets have been extensively studied, because of rich frustrated magnetism expected on the simple 2D Bravais lattice. Theoretically, it has gained a consensus that the ground state for the nearest-neighbor antiferromagnetic (AF) Heisenberg model

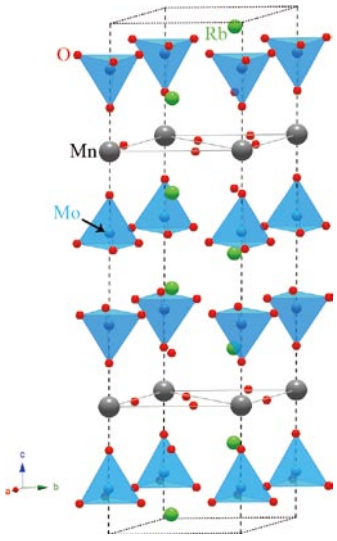

Fig. 1. Crystal structure of $Rb_4Mn(MoO_4)_3$ with equilateral triangular lattices of Mn^{2+} and MoO_4 tetrahedra.

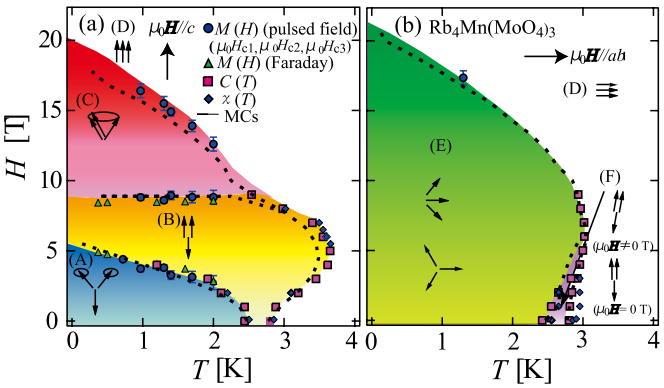

Fig. 2. *H-T* phase diagrams of $Rb_4Mn(MoO_4)_3$ for (a) μ_0H // *c* and (b) μ_0H // *ab* constructed by using various experimental techniques, and by Monte Carlo simulations.

has the 120° spin order. In this case, the concept of vector spin chirality, the handedness of the way the spins are rotated in a 120° order for a given triangle, may become essential and lead to exotic phenomena such as phase transitions with a new universality class and multiferroic phenomena. However, neither detailed study of the phase diagram under external field nor quantitative comparison between experiment and theory has been made so far, because of a relatively large scale of the antiferromagnetic coupling *J* and/or lattice deformation due to magnetostriction.

Recently, we have succeeded in growing single crystals of the quasi-2D Heisenberg triangular antiferromagnet $Rb_4Mn(MoO_4)_3$ and investigated its magnetic properties [3]. Powder neutron diffraction measurements confirmed that the structure is consistent with the X-ray results and stable down to 1.5 K. Thus, $Rb_4Mn(MoO_4)_3$ has the equilateral triangular lattice formed by Mn^{2+} with S = 5/2 (Figure 1). We have made a comprehensive study on the crystal/spin structures and thermodynamic properties of the quasi-2D Heisenberg triangular antiferromagnet $Rb_4Mn(MoO_4)_3$ [3]. This material exhibits the successive transitions and 1/3 magnetization plateau phase under field, reflecting its easy-axis anisotropy. As a rare case in geometrically frustrated magnets, quantitative agreement between experiment and theory has been found for the phase diagrams (Figure 2) and magnetic properties, establishing the system as a model 2D Heisenberg triangular antiferromagnet characterized by the nearest neighbor Heisenberg Hamiltonian.

Our detailed quantitative agreement between experiment and theory for this geometrically frustrated magnet has established $Rb_4Mn(MoO_4)_3$ as a model system to explore many unusual aspects of 2D frustrated magnetism, such as critical dynamics associated with vector chirality, multiferroic noncolliner magnetism, and instability of conventional magnon excitations.

References
[1] S. T. Bramwell and M. J. P. Gingras, Science **294**, 1495 (2001).
[2] H. Kageyama, K. Yoshimura, R. Stern, N. V. Mushnikov, K. Onizuka, M. Kato, K. Kosuge, C. P. Slichter, T. Goto, and Y. Ueda, Phys. Rev. Lett. **82**, 3168 (1999).
[3] R. Ishii, S. Tanaka, K.Onuma, Y. Nambu, M. Tokunaga, T. Sakakibara, N. Kawashima, Y. Maeno, C. Broholm, D. P. Gautreaux, J. Y. Chan, and S. Nakatsuji, Europhy. Lett. **94**, 17001 (2011).

Authors
R. Ishii, S. Tanaka, K. Onuma[a], Y. Nambu, M. Tokunaga, T. Sakakibara, N. Kawashima, Y. Maeno[a], C. Broholm[b], D. P. Gautreaux[c], J. Y. Chan[c], and S. Nakatsuji
[a]Kyoto University
[b]Johns Hopkins University
[c]Louisiana State University

Magnetic Control of Chiral Domains in the Chiral Spin States of $Pr_2Ir_2O_7$

Nakatsuji Group

Electronic transport under the influence of a background spin texture opened fundamental themes in physics, such as giant/colossal magnetoresistive effects, and the anomalous Hall-effect (AHE). These magnetotransport phenomena provided the conceptual basis for current research in spintronics and have so far been intensively investigated in ferromagnetic, transition metals, oxides, and semiconductors. The recent discovery of a chiral spin liquid in the metallic frustrated magnet $Pr_2Ir_2O_7$ [refs. 1, 2] through the AHE at zero magnetic field below 1.5 K, provides a unique laboratory for studying novel magnetotransport phenomena in the absence of magnetic dipole long range order [1-3].

In this study, we uncover a strong anisotropy in both the AHE and the magnetoresistance of the chiral spin states observed in cubic single crystals of $Pr_2Ir_2O_7$ [4]. Hysteresis in the AHE appearing below 1.5 K, is most pronounced when the magnetic field is cycled along the [111] direction, as shown in Fig. 1. This indicates that delocalized orbital currents generating an associated magnetic moment and which are linearly coupled to the chiral order parameter breaking the parity and time-reversal invariance, circulate within the [111] kagome planes. The hysteresis loop in the AHE characterizing the chiral spin state, closes at a metamagnetic transition critical field B_c observed only for fields along the [111] direction. These observations pose the intriguing possibility that Dirac magnetic monopoles and antimonopole, which are deconfined and interact through the magnetic Coulomb law in the classical dipolar spin ice, now have a finite quantum-mechanical average in the zero-field chiral spin-liquid state which is dominated by 2-in, 2-out spin-ice configurations. Above B_c and only for fields applied along the [111] direction, we observe a large positive magnetoresistance and Shubnikov de Haas oscillations. This suggests that densely populated magnetic monopoles and antimonopoles, reconstruct the electronic structure of the Ir conduction electrons in the basal kagome planes.

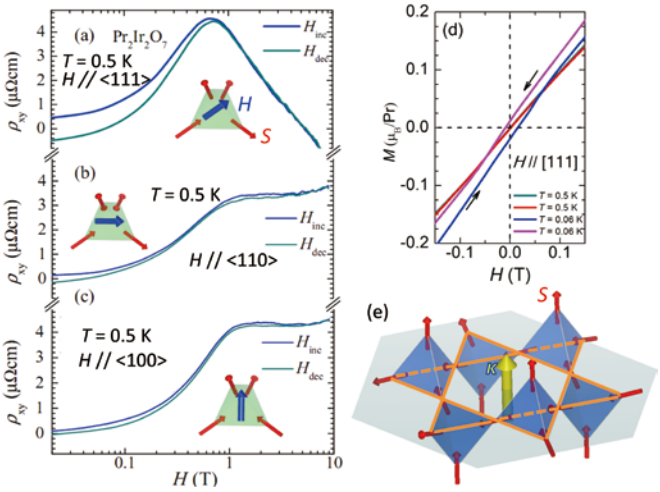

Fig. 1. Hall resistivity $\rho_{xy} = R_{xy} \cdot t$, where t is the sample thickness, for a $Pr_2Ir_2O_7$ single crystal, as a function of magnetic field H applied respectively along the (a) [111], (b) [110], and (c) [100] crystallographic directions and for T = 500 mK, respectively. These traces were measured for increasing (blue traces) and decreasing (gray traces) field scans. Notice how the hysteresis depends strongly on the orientation of the magnetic-field. (d) Magnetization as a function of H, for increasing and decreasing field scans, and respectively for T = 0.06 and 0.5 K[7] [ref.3]. Notice the absence of hysteresis among the traces acquired at T = 0.5 K, but its presence in the Hall response acquired at the same temperature, as shown in (a). (d) A schematic picture to show the fictitious field $\boldsymbol{K}$ // [111], generating delocalized orbital currents within the [111] kagome planes, which are linearly coupled to the chiral order parameter breaking the parity and time-reversal invariance.

References

[1] S. Nakatsuji, Y. Machida, Y. Maeno, T. Tayama, T. Sakakibara, J. van Duijn, L. Balicas, J. N. Millican, R. T. Macaluso, and Julia Y. Chan, Phys. Rev. Lett. **96**, 087204 (2006).
[2] Y. Machida, S. Nakatsuji, Y. Maeno, T. Tayama, T. Sakakibara, and S. Onoda, Phys. Rev. Lett. **98**, 057203 (2007).
[3] Y. Machida, S. Nakatsuji, S. Onoda, T. Tayama, and T. Sakakibara, Nature, **463**, 210 (2010).
[4] L. Balicas, S. Nakatsuji, Y. Machida, and S. Onoda, Phys. Rev. Lett. **106**, 217204 (2011).

Authors
S. Nakatsuji, L. Balicas[a], Y. Machida[b], and S. Onoda[c],
[a]National High Magnetic Field Laboratory, Florida State University
[b]Tokyo Institute of Technology
[c]RIKEN

Discovery of Zero-Field Quantum Critical Point in the Heavy Fermion Superconductor β-$YbAlB_4$

Nakatsuji and Sakakibara Groups

Singularities where the smoothness of physical laws breaks down and is replaced by mathematical infinities are studied extensively in physics as sources of fascinating new forms of behavior. For instance, lightning bolts, tornadoes and black holes are show-cases of singularities in physics. In the past few decades, it has been recognized that similar singularities also develop inside "ordinary" materials at low temperatures, and when they do, a new kind of emergent phenomena appears. In particular, the electron fluid that carries electricity in metals becomes unstable. For the past 80 years, Fermi liquid theory, which is the idealized picture of electron liquid, has provided a mainstay of our understanding of metals. However, in β-$YbAlB_4$, a new ytterbium-based material, this picture breaks down, revealing an underlying singularity at zero temperature i.e. quantum critical point (QCP) [1,2].

In order to study a singularity in a material (QCP), a tuning of a physical parameter such as temperature, magnetic field, pressure, and doping is necessary to make the material approaches to QCP in the phase space. This can be compared to traveling around space and time searching black holes. However, like the black hole forms around a singularity masking the mathematical singularity at its center in the fabric of space and time, the breakdown of the Fermi liquid picture in β-$YbAlB_4$ is masked by superconductivity which prohibits any direct measurement of the underlying metallic state [2,3]. Moreover, the singularities have

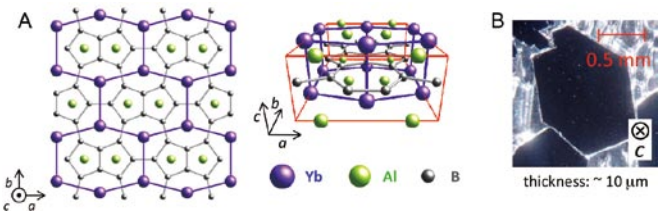

Fig. 1. A) Crystal structures of β-$YbAlB_4$. B) A picture of single crystals of β-$YbAlB_4$.

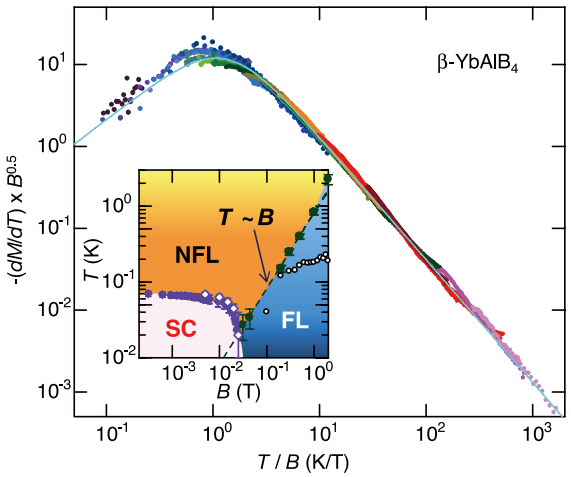

Fig. 2. Scaling observed for the magnetization at $T \lesssim 3$ K and $B \lesssim 2$ T. Here, the magnetization M satisfies a scaling equation $-dM/dT = B^{-1/2}f(T/B)$ over a wide range of temperature and field shown in the inset. This means that the physical properties around QCP are determined only by the ratio T/B. In addition this proves that the QCP is located just at zero-magnetic field. Inset shows the B-T phase diagram of β-YbAlB$_4$ in the low T and B region. The filled circles are determined from the peak temperatures of $-dM/dT$, below which the FL ground state is stabilized. At low field, the thermodynamic boundary between the FL and NFL regions is on a $k_BT \sim g\mu_BB$ line (broken line). The open circles are the temperature scale T_{FL}, below which the T^2 dependence of the resistivity is observed [1].

often been obscured by disorder. For all these difficulties, we have succeeded in probing deep inside the singularity using the ultrapure form of the crystals and high fidelity magnetization measurements [2]. As a result, we have found that the magnetization M satisfies a scaling equation $-dM/dT = B^{-1/2}f(T/B)$ over a wide range of temperature and field at $T \lesssim 3$ K and $B \lesssim 2$ T. In other words, this means that the singularity lets its presence be known by affecting the material properties at elevated temperatures and magnetic fields, several orders of magnitude larger than the boundaries of the superconducting domain. It bears resemblance to a black hole, which cannot be probed directly, but whose gravitational pull is felt by the surrounding stars, long distances away. The T/B scaling proves not only unconventional quantum criticality but, furthermore, that the singularity in β-YbAlB$_4$ occurs just at zero magnetic field with an experimental error comparable to Earth's magnetic field at ambient pressure.

This is quite surprising compared to canonical QCP materials which require a tuning of a control parameter to approach QCP. This raises an intriguing possibility that this metal may be part of a new, quantum critical, phase of matter *i.e.* the spontaneous quantum criticality in β-YbAlB$_4$ would persist in a finite region of the phase-space, as a function of pressure or doping [2]. This strange state, which displays an intriguing correspondence of self-similarity under applied magnetic field and temperature, can be viewed as the third state of the matter in addition to the Fermi liquid and a superconductor. It is expected that this observation opens new horizons in our understanding of quantum criticality and provides us with important information which can help shed light on the strange metal state and superconductivity not only in this material, but also in other families of unconventional superconductors.

References

[1] S. Nakatsuji, K. Kuga, Y. Machida, T. Tayama, T. Sakakibara, Y. Karaki, H. Ishimoto, S. Yonezawa, Y. Maeno, E. Pearson, G. G. Lonzarich, L. Balicas, H. Lee, and Z. Fisk, Nature Physics **4**, 603 (2008).
[2] Y. Matsumoto, S. Nakatsuji, K. Kuga, Y. Karaki, N. Horie, Y. Shimura, T. Sakakibara, A. H. Nevidomskyy, and Piers Coleman, Science **331**, 316 (2011).
[3] K. Kuga, Y. Karaki, Y. Matsumoto, Y. Machida, and S. Nakatsuji, Phys. Rev. Lett. **101**, 137004 (2008).

Authors
Y. Matsumoto, S. Nakatsuji, K. Kuga, Y. Karaki, N. Horie, Y. Shimura, T. Sakakibara, A. H. Nevidomskyya[a,b], and Piers Coleman[a, c]
[a]Rutgers University
[b]Rice University
[c]Royal Holloway, University of London

Broken Inversion Symmetry in Metallic Pyrochlores $A_2Re_2O_{7-x}S_x$

Ohgushi, Sakakibara, Yagi, and Y. Ueda Groups

Occasionally, the inversion symmetry in a solid is spontaneously broken. The most famous example of this phenomenon is ferroelectrics. It is by now common knowledge that the covalency plays a crucial role in stabilizing the ferroelectricity. The mechanism of room temperature ferroelectricity in $PbTiO_3$, which is in marked contrast to the ferroelectric phase below 85 K in $CdTiO_3$, is ascribed to the stronger covalency of the Pb-O bonds than Cd-O bonds. In contrast to the insulating nature of ferroelectrics, there is a class of materials categorized as a metallic state without the inversion symmetry, which is sometimes called a noncentrosymmetric metal or a polar metal. Since itinerant electrons screen the electric field, the physics does not exactly parallel that of ferroelectrics. For example, the primary order parameter characterizing the phase is no longer the ferroelectric polarization, but rather a quantity related to the loss of the inversion center, *e.g.* a second-rank pseudotensor. Moreover, instead of dielectric properties, transport properties are the focus of discussion. In the inversion-broken metal, any electronic states near the Fermi energy can no longer be classified according to the parity. This parity mixing of the Wannier function gives rise to intriguing transport phenomena such as the inverse Faraday effect. Concerning the phase stability, there is no study which unravels the role of the covalency.

We have investigated structural and electronic properties of pyrochlore-type $A_2Re_2O_{7-x}S_x$ (A = Ca, Cd, and Pb)

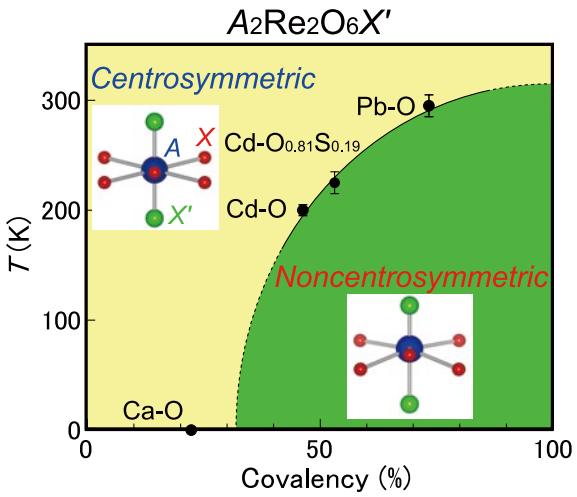

Fig. 1. Electronic phase diagram for pyrochlore-type compounds $A_2Re_2O_{7-x}S_x$. Structural transition temperature associated with a loss of inversion symmetry is plotted against the covalency of the A-X' bonds $f_{cov} = \exp(-\Delta\chi^2/4)$, where $\Delta\chi$ is the difference of electronegativity between A and X' elements.

[1]. These compounds exhibit a unique structural transition characterized by a loss of the inversion symmetry in a metal. As can be clearly seen from Fig. 1, the material variation of the transition temperature is well sorted by the covalency of a particular bond *A*-*X'* in the pyrochlore-type compounds $A_2B_2X_6X'$. How the covalent *A*-*X'* bonds break the inversion symmetry is well interpreted for *A* = Pb. Pb^{2+} ions with a stereochemical active lone pair ($6s^2$ electrons) prefer a distorted metal coordination with two-types of covalent *A*-*X'* bonds of the different bond length (inset of Fig. 1). This local breakdown of inversion symmetry spreads over the global lattice, because the *A* site is the inversion center in the space group of centrosymmetric phase. Our results clearly indicate that the mechanism of the structural instability has a common feature among ferroelectrics and noncentrosymmetric metal. On the other hand, we have also found an anomalous one-to-one correspondence in the resistivity: incoherent behavior in the centrosymmetric phase and coherent behavior in the noncentrosymmetric phase. This infers an existence of unusual coupling between the charge and lattice degrees of freedom in noncentrosymmetric metal, which should be clarified in a future study.

Reference
[1] K. Ohgushi, J. Yamaura, M. Ichihara, Y. Kiuchi, T. Tayama, T. Sakakibara, H. Gotou, T. Yagi, and Y. Ueda, Phys. Rev. B **83**, 125103 (2011).

Authors
K. Ohgushi, J. Yamaura, M. Ichihara, Y. Kiuchi, T. Tayama, T. Sakakibara, H. Gotou, T. Yagi, and Y. Ueda

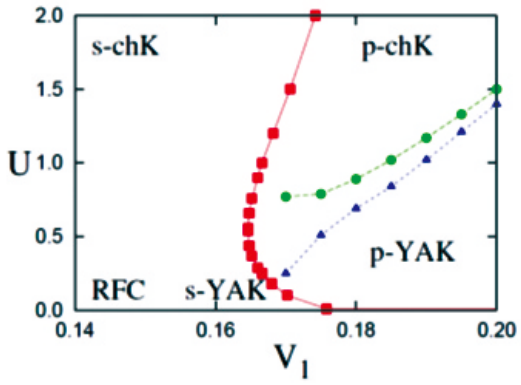

Fig. 1. Phase diagram in the parameter space of the phonon assisted hybridization with the p-wave conduction electrons, V_l, and the Coulomb interaction, U [2]. The left region is characterized by the s-type energy spectra and the right one by the p-type ones. At the boundary, the energy spectrum is of the two-channel Kondo type. The lower left corner of the parameter space is characterized by the renormalized Fermi chain.

Kondo Effect of a Vibrating Magnetic Ion in a Metal

K. Ueda Group

When an ion is placed in a cage structure with its radius being smaller than the size of the cage, vibrations of the ion show strong anharmonicity. Such phenomena are observed in filled skutterudites, β-pyrochlore, and clathrate compounds and are believed to be responsible for certain unusual properties of these materials.

When a magnetic ion is placed in the sea of conduction electrons, electrons in the localized orbital of the magnetic ion hybridize with the conduction electrons. This coupling is the origin of the conventional Kondo effect. On the other hand, in the case of a nonmagnetic ion, conduction electrons are scattered by vibrations of the ion. Yu and Anderson have shown that a different type of Kondo effect is possible when the electron-phonon coupling is strong.

To discuss Kondo effect of a vibrating magnetic ion in the sea of conduction electrons, a generalized Anderson model is derived for the harmonic confinement potential [1, 2]. The model includes a new channel of hybridization associated with phonon emission and absorption. In the simplest case of the localized electron orbital with the s-wave symmetry, hybridization with p-waves becomes possible. An interesting interplay among the conventional s-wave (s-chK) and the p-wave Kondo (p-chK) effects and the Yu-Anderson-type Kondo (YAK) effect is found. The ground state phase diagram is determined by using the numerical renormalization group method, which is shown in Fig. 1. Two different types of stable fixed points are identified and the two-channel Kondo fixed points generically realized at the boundary.

Effect of anharmonicity of a cage potential for a magnetic ion is also studied by us and will be published in a separate paper [3].

References
[1] S. Yashiki, S. Kirino, and K. Ueda, J. Phys. Soc. Jpn. **79**, 093707 (2010) .
[2] S. Yashiki, S. Kirino, K. Hattori, and K. Ueda, J. Phys. Soc. Jpn. **80**, 064702 (2011).
[3] S. Yashiki and K Ueda, submitted to J. Phys. Soc. Jpn.

Authors
S. Yashiki and K. Ueda

Quantum Critical Phenomena of Helium 4 in Nanoporous Media

Oshikawa Group

Liquid Helium 4 becomes a superfluid at very low temperatures. In atmospheric pressure, the superfluid transition occurs at 2.14 K. This is a remarkable example of phase transition. Superfluid is a quantum state of matter, and its existence reflects the strong quantum fluctuations in liquid Helium 4. On the other hand, however, the superfluid transition itself is classical, belonging to the same universality class as the phase transition in the 3-dimensional classical XY spin model. In general, a phase transition at finite temperature is ultimately a classical phase transition, even if it is caused by quantum effects. In bulk liquid Helium 4, the transition temperature depends weakly on the pressure, but there is no essential change up to the pressure where the Helium 4 solidifies.

The situation could change drastically when the liquid Helium 4 is confined in porous media. In earlier studies, liquid Helium 4 was filled in Vycor glass, which is a porous material with typical pore diameter of approximately 6 nm. The superfluid transition temperature was suppressed by the confinement, but there was still no essential change. Recently, experiments were carried out [1] using a new porous material, Gelsil glass, with smaller pores. It has typical pore diameter of 2.5 nm. The superfluid transition

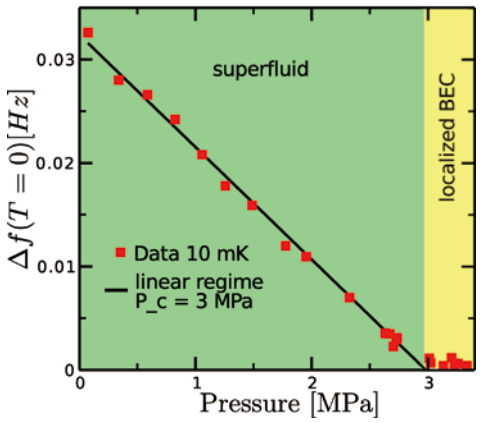

Fig. 1. Superfluid density extrapolated to zero temperature and as a function of the pressure. The experimental data, shown in squares, are taken from Ref. [1]. The solid line is the 4-dimensional XY linear scaling, which shows a remarkable agreement with the data except in the close vicinity of the QCP.

temperature is suppressed strongly, and goes down to zero under pressure.

We studied this novel setting of superfluid transition theoretically [2]. First, we clarified why the Gelsil system behaves so differently from the previously studied systems such as Vycor. We found that, the energy scale of the phase fluctuation due to the confinement is inversely proportional to the effective pore volume. As a consequence, we found that, quantum fluctuations become important only below 0.005 K in Vycor, but already below 1.4 K in Gelsil. This is consistent with the observed difference between Vycor and Gelsil.

The phase transition at zero temperature is a quantum phase transition. It accompanies quantum critical phenomena, which control physics also at finite temperatures. We studied physical properties of the system, from this point of view. The system has randomness, owing to random distribution of pores and their sizes. The system can be modeled by the Bose-Hubbard model or quantum rotor model. While it has been known in these models that the particle-hole symmetry is broken except at special multicritical points, we pointed out that the particle-hole symmetry is effectively restored because of the randomness. As a result, the quantum critical phenomena belong to 4-dimensional XY universality class, the extra one dimension corresponding to the quantum fluctuations.

Assuming 4-dimensional XY universality class, we can derive scaling for several physical quantities. The superfluid density at zero temperature is predicted to scale linearly with the pressure. As shown in Fig. 1, this agrees very well with the experimental data, except for the close vicinity of the quantum critical point where the randomness changes the critical behavior. The quantum critical phenomena also govern the critical temperature; although the phase transition itself at finite temperatures is classical, its dependence on the pressure is determined by quantum critical scaling. The theoretical prediction that the square of the critical temperature behaves linearly in the pressure matches well with the experimental data, as in Fig. 2. In conclusion, we have shown that the small pore size of Gelsil leads to strong quantum fluctuations in confined liquid Helium 4, and the low-temperature physics can be largely understood as quantum critical phenomena belonging to 4-dimensional XY universality class.

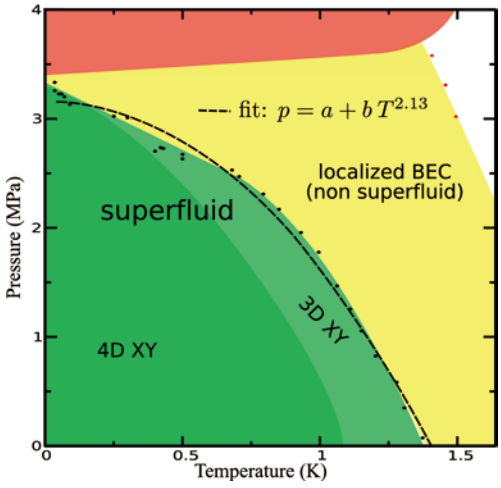

Fig. 2. The phase diagram in temperature-pressure plane. The transition curve is fitted by power-law. The result is consistent with the 4-dimensional XY critical behavior (proportional to T^2)

References

[1] K. Yamamoto, H. Nakashima, Y. Shibayama, and K. Shirahama, Phys. Rev. Lett. **93**, 075302 (2004)

[2] T. Eggel, M. Oshikawa, and K. Shirahama, arXiv:1004.4004

Authors

T. Eggel, M. Oshikawa, and K. Shirahama[a]

[a]Keio University

Electronic Transport in Frustrated Systems

Tsunetsugu Group

Frustrated systems have been intensively studied both experimentally and theoretically for several decades. Main targets of these studies are traditionally antiferromagnetic spin systems, both classical and quantum, on geometrically frustrated lattices, and typical examples are Heisenberg spins on triangular, kagome, and pyrochlore lattices. Frustration effects would be also important in itinerant electron systems, when charge fluctuations are strongly suppressed due to large Coulomb repulsion, U. Electron correlations depend strongly on local spin configurations, and thus spin frustrations have large effects on quasiparticle and charge dynamics. Mott metal-insulator transition is a typical phenomenon of this sort. Change in charge dynamics near the Mott transition is manifested in the frequency dependence of optical conductivity σ(ω). The organic triangular-

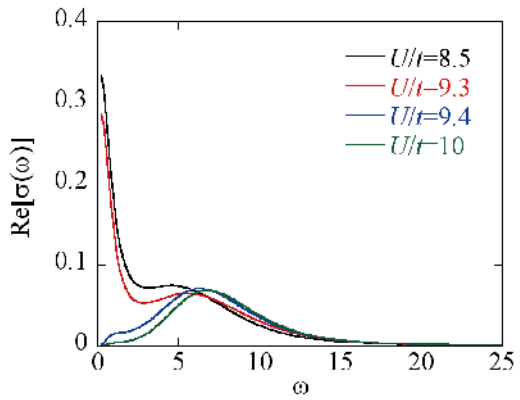

Fig. 1. Optical conductivity of the Hubbard model on triangular lattice at temperature T=0.09t. Units of ω is t.

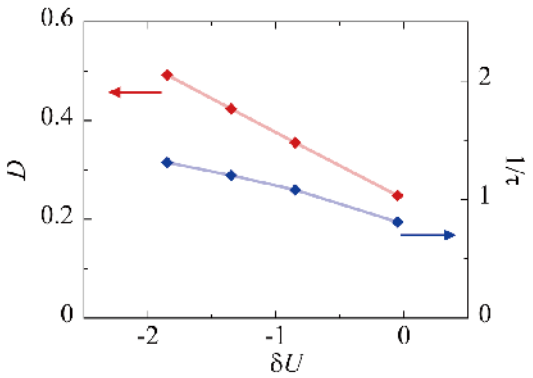

Fig. 2. Weight D and width $1/\tau$ of the Drude part of $\sigma(\omega)$ near the critical point. $\delta U = U - 9.35t$. Note that $D=0$ for $\delta U > 0$.

lattice compound κ-$(ET)_2$-$Cu_2(CN)_3$ exhibits spin-liquid like behaviors at low temperatures. It is quite unusual that $\sigma(\omega)$ shows no distinct gap structure but a pseudogap-like nature, continuous distribution of optical weight below the charge transfer gap of ~2 eV [1]. This is in sharp contrast with the result for the antiferromagnetically ordered related material κ-$(ET)_2$-Cu[$N(CN)_2$]Cl, which exhibits a clear gap of ~0.1 eV.

To investigate charge transport in frustrated itinerant electron systems, we numerically calculate the optical conductivity of the half-filled Hubbard model on the regular triangle lattice near the critical end point of the Mott transition. To take into account strong correlation effects and short-range frustration, we have employed a cluster dynamical mean field theory (CDMFT) with a three-site cluster. For calculating electron Green functions, we need a powerful impurity solver for the highly frustrated and correlated system and developed an effective continuous-time quantum Monte Carlo (CTQMC) program based on strong coupling expansion, which is tailored for the lattice symmetry. After obtaining self-consistent Green functions, we evaluate the current-current correlation function and determine optical conductivity $\sigma(\omega)$.

Most interesting is the behavior near the critical end point (U_c, T_c) of the Mott transition in the parameter space of Coulomb repulsion U and temperature T. Figure 1 shows evolution of the Mott-Hubbard gap in the frequency dependence of $\sigma(\omega)$ when U is increased at a temperature near T_c. t is the electron transfer integral. As is known for other frustrated systems, because of strong frustration effects, the critical temperature is only 1% of the total band width of the noninteracting system. The critical value U_c/t is slightly larger than 9.3, and no magnetic instability is observed near the critical point. Coherent quasiparticle transport is manifested by a Drude peak in the low-ω region on the metallic side ($U/t \leq 9.3$). The Drude peak disappears rapidly upon increasing U further into the insulating side, while a broad peak at higher frequencies around $\omega \sim 6t$ is robust. This incoherent peak is the contribution of the Hubbard band, which is checked by analysis of electron spectral function. It is remarkable that a slight increase of U leads to the drastic change in the coherent transport, and this is characteristic to frustrated systems.

We performed detailed analysis about the coherent part. We separated the coherent part from the whole $\sigma(\omega)$ and determined the Drude weight D and the peak width $1/\tau$. Figure 2 shows these values as a function of U, and the result reveals two interesting features. The first point is that the peak width decreases with approaching the metal-insulator transition point, and this is opposite to usual expectation based on the picture that quasiparticle dynamics loses coherence at the transition. The second point is that the Drude weight seems to vanish nonlinearly in δU. This indicates the scaling behavior, $D \sim (\delta \sim U)^{\mu}$, with a quite small exponent μ. This is consistent with an analysis based on the extended Drude form, which shows that the metal-insulator transition is dominated by the increase of effective mass rather than change in life time. We believe that these results are important universal characters of electron transport near the Mott transition, and more systematic analysis is in progress including examination of the effects of current vertex correction.

Reference

[1] Kézsmárki *et al.*, Phys. Rev. B **74**, 201101 (2006)

Authors
H. Tsunetsugu, T. Sato and K. Hattori

Novel Microwave Resonances around Integer Landau Level Fillings in Unidirectional Lateral Superlattices

Iye Group

Microwave conductivity has recently proven to be a powerful tool to investigate electron-solid-like ground states, the Wigner crystal (WC) [1] and the charge-density-wave (CDW) [2,3] states, of a two-dimensional electron gas (2DEG) subjected to a quantizing magnetic field. Resonant peaks observed in the frequency dependence of the conductivity are interpreted as the pinning modes of WC or CDW. The study of these electron phases usually requires ultrahigh mobility 2DEGs (mobility $\mu > 1{,}000$ $m^2V^{-1}s^{-1}$), since these fragile states are otherwise readily destroyed by disorder. Conversely, WC or CDW states are expected to be corroborated by artificially introduced periodic potential modulation having the period matching with the inherent period of these electron-solid-like states. In fact, anisotropic dc resistivity suggesting the formation of the unidirectional CDW (stripe) phase has been reported in a short period (~100 nm) unidirectional lateral superlattice (ULSL) fabricated from a 2DEG with a modest mobility ($\mu \sim 100$ $m^2V^{-1}s^{-1}$) [4].

We have performed the microwave conductivity measurement on ULSLs to explore the electron-solid-like states

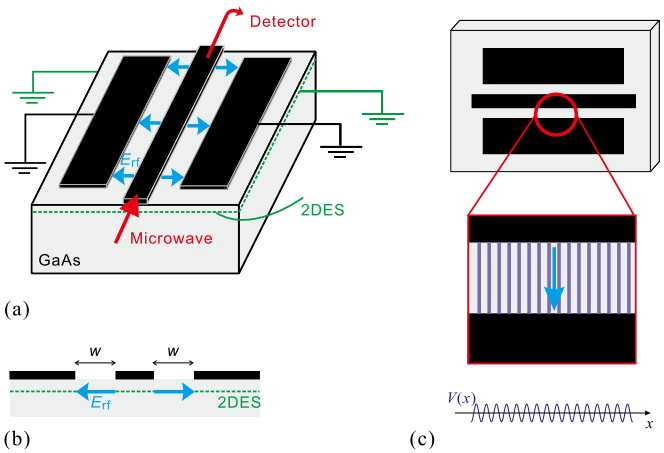

Fig. 1. (a) Schematic diagram of the sample, with the CPW depicted by black plates. (b) Cross sectional view. (c) Periodic modulation $V(x)$ introduced into the 2DEG beneath the slots.

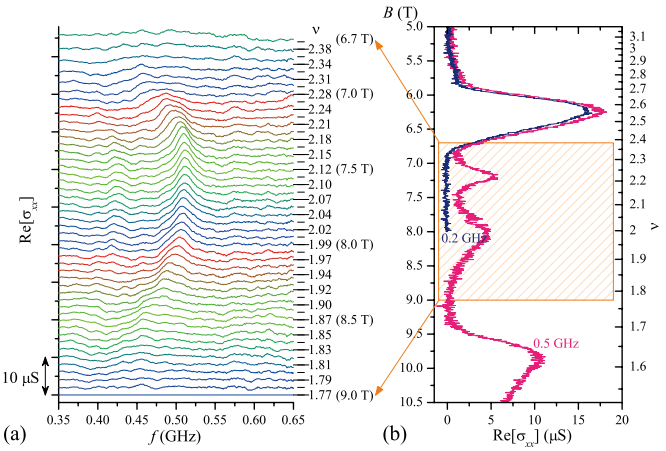

Fig. 2. (a) Spectra of Re[σ_{xx}] measured at fixed fillings ν (fixed magnetic fields B) noted on the right. Successive traces (taken by the decrement step of 0.05 T) are offset by 2 μS for clarity. (b) Magnetic-field dependence of Re[σ_{xx}] at fixed frequencies (corresponding to the vertical cross section of (a)): on resonance (0.5 GHz) and off resonance (0.2 GHz). The hatched rectangle indicates the magnetic field range the spectra in (a) are acquired.

induced by the unidirectional modulation. The schematic of the sample is shown in Fig. 1. A metal film coplanar waveguide (CPW) is patterned onto the surface of GaAs/AlGaAs 2DEG wafer having the mobility μ = 102 $m^2V^{-1}s^{-1}$ (Fig. 1(a)). The microwave propagating along the CPW is attenuated by coupling with the 2DEG underlining the gap between the metallic gates (Fig. 1(b)). Thus, the power transmission P through the CPW is the measure of (the real part of) the diagonal conductivity Re[σ_{xx}] of the 2DEG underneath the slots, with the relation Re[σ_{xx}] = $-w/(2lZ_0)\ln(P)$, where l = 1.6 mm is the CPW length, w = 2.8 μm is the slot width, and Z_0 = 50 Ω is the line impedance [1-3]. As shown in Fig. 1 (c), a unidirectional periodic potential modulation (with the period a = 200 nm) is introduced into the 2DEG beneath the slots via strain-induced piezoelectric effect by placing a grating of electron-beam resist on the surface. The expected role of the periodic modulation is two-fold: (1) to stabilize the CDW (stripe) state, and (2) to provide well-defined pinning potential.

Our central finding is presented in Fig. 2 [5]. A resonant peak is observed at ~0.5 GHz in the vicinity of the integer Landau level filling ν = 2. As can be seen in Fig. 2 (a), the peak is observed in a rather narrow filling factor range 1.84 < ν < 2.31, and the peak frequency f_{pk} slightly shifts to the lower frequency side as the filling departs away from the integer value. Similar but weaker resonances are also observed around ν = 3 and 4. The resonances are absent in the reference sample without the periodic modulation and therefore can be unambiguously ascribed to the effect of the modulation.

The exact origin of the resonant peak is not specified at present, but its resemblance to the pinning mode of WC [1], as well as the high Q-factor $Q = f_{pk}/\Delta f$ ~20 (with Δf the full width at half maximum), suggests that the peak represents the pinning mode, in the artificially introduced pinning potential, of a certain electron-solid-like state (presumably the stripe state) induced by the periodic modulation.

References

[1] Y. Chen *et al*., Phys. Rev. Lett. **91**, 016801 (2003).
[2] R. M. Lewis *et al*., Phys. Rev. Lett. **89**, 136804 (2002).
[3] G. Sambandamurthy *et al*., Phys. Rev. Lett. **100**, 256801 (2008).
[4] A. Endo and Y. Iye, Phys. Rev. B **66**, 075333 (2002).
[5] T. Kajioka, A. Endo, S. Katsumoto, and Y. Iye, Proc. 30-th Int. Conf. Phys. Semiconductors (2010) (to be published).

Authors
T. Kajioka, A. Endo, S. Katsumoto, and Y. Iye

Control of Rectification with Current Injection in (Ga,Mn)As Tri-Layer Tunnel Junctions

Katsumoto Group

In metallic magnetic tunnel junctions (MTJs), rectification of microwaves driven by ferromagnetic resonance (FMR) has been reported [1]. In semiconductor devices, rectification functionality can be naturally obtained through space-charge polarity, hence, some additional functionalities are expected in diluted magnetic semiconductor (DMS) devices. In this paper, we report control of rectification in (Ga,Mn)As magnetic tunnel junctions (MTJs) both by magnetic field and current injection.

The layered structure of triple (Ga,Mn)As magnetic tunneling junction (MTJ) is schematically shown in the inset of Fig. 1. The center layer is thinner than the other two and has smaller coercivity. The ferromagnetic transition temperature estimated from appearance of tunneling magnetoresistance (TMR) is about 40K. The film was cut into pillars with cross section of 1.4×0.9 μm^2 rectangle along [100]. The measurements were done at 4.2 K with field cooling of 0.7 T along [100]. AC bias above 100 kHz was applied through a coplanar waveguide (CPW) placed under the substrates and below 1 kHz through ordinal cryogenic wires.

Figure 1 also shows resistance jumps following 1 mA – 2 sec. current injections. As reported in [2], the junction resistance jumps up to different values depending on the current direction and switching between these two states just by the current injection is possible. The current threshold is 3 ×10^4 A/cm^2 which is comparable to or lower than reported in [2] though the pulse width of 3 ms is required in the present devices.

Rectified voltage was detected with a differential amplifier and an example of response to external magnetic field is shown in Fig. 2 for the frequency of 1.4 GHz. Each jump in the output voltage has a corresponding one in the resistance manifesting that the discontinuity is due to transitions in configuration of magnetization. However the voltage is not

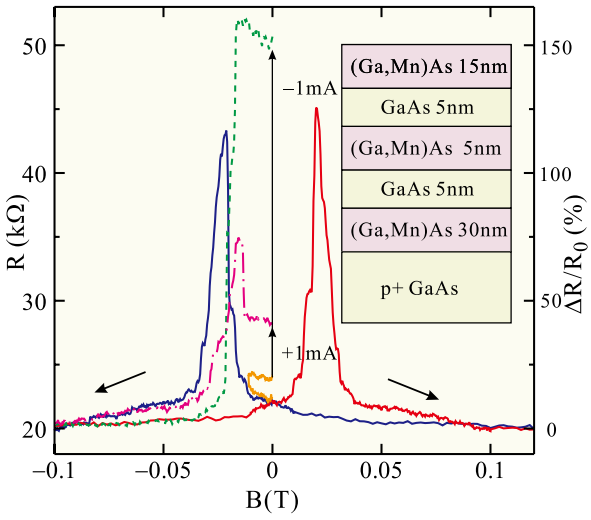

Fig. 1. Typical TMR and the cross section of the layered structure. Mn content is 4%. Vertical arrows indicate resistance jumps due to pulsed current injection.

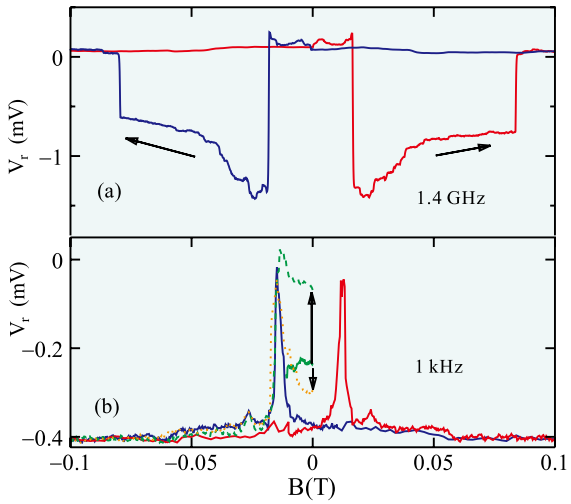

Fig. 2. Rectified voltage signals for different two samples. (a) Sample A with 1.4GHz 0dBm attenuation through CPW, which shows sign reversal. (b) Sample B with 1kHz direct AC modulation.

simple reflection of resistance change. In the case of Fig. 2 (a), the sign of rectification is reversed at the field range around the resistance peaks. It is more dramatic in Fig. 2 (b), where largest peaks in the output appear not at the resistance peaks but at small shoulders. Note that the response to magnetic field has no dependence on modulation frequency, which eliminates FMR-driven rectification. The results can rather be understood by simple Julliere model with modification in energy dependence of spin-subband density of states [3].

Figure 2 also displays jumps of the rectified voltage with injection of current (1 mA, 2 s). The direction of the jump is reversed with current inversion. And we note that cyclic sign reversal of rectification by spin injection is possible in the present devices, which implies potential applications to, *e.g.*, multiple signal superposition on microwaves etc.

References
[1] A. A. Tulapurkar *et al.*, Nature **438**, 339 (2005).
[2] M. Watanabe *et al.*, Appl. Phys. Lett. **92**, 262 (2008).
[3] Y. Hashimoto, H. Amano, Y. Iye, and S. Katsumoto, Appl. Phys. Express (in press).

Authors
Y. Hashimoto, H. Amano, and S. Katsumoto

Extrinsic Spin Hall Effect Induced by Iridium Impurities in Copper

Otani Group

The generation of pure spin currents, flows of only spin angular momentum without charge current, should play an important role in the next generation spintronic devices. The spin Hall effect (SHE) is one of the promising ways to create pure spin currents in nonmagnetic materials without using ferromagnets. Large SHEs have been recently found in noble metals such as Pt and Au and this has triggered an important effort of research on the SHE in metallic materials. The mechanism of such large SHEs, however, has not been figured out yet; whether it is intrinsic or extrinsic, if it is extrinsic whether it stems from the skew scattering mechanism or the side jump one. In this work, we focus on the extrinsic SHE; by adding Ir impurities into a pure Cu wire,

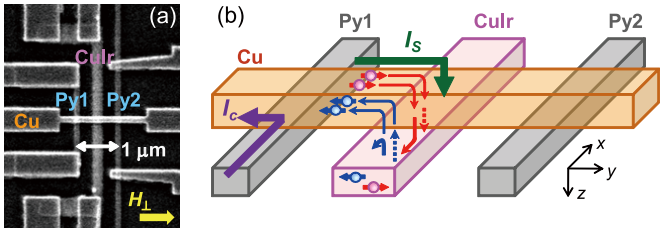

Fig. 1. (a) Scanning electron microscopy image of a spin Hall device consisting of two Py wires and a CuIr middle wire bridged by a Cu wire. (b) Schematic of the mechanism of ISHE due to the spin absorption effect.

we have studied the impurity concentration dependence of the SHE in CuIr alloys. The final goal of the present study is to identify if the major contribution to the SHE is the skew scattering by the Ir impurities and what is the magnitude of the spin Hall (SH) angle which represents the maximum yield of the transformation of charge into spin current density.

In the present study, we have adopted the spin absorption method using a lateral spin valve structure which consists of two Permalloy (Py) wires and a CuIr middle wire bridged by a Cu wire, as shown in Fig. 1 (a). This method is quite powerful for SHE measurements in materials with short spin diffusion length. We perform inverse SHE (ISHE) measurements where pure spin currents generated from Py1 are absorbed into the CuIr middle wire and the deflection in the same direction of the opposite spin-up and spin-down electrons can be detected (see Fig. 1(b)). In order to obtain the SH angle of CuIr, we have to also evaluate its spin diffusion length as well as the spin absorption rate into the CuIr wire. This can be done by measuring the spin valve effect between the two Py wires with and without the CuIr wire (not shown here).

Figure 2 shows the obtained SH resistivity (ρ_{SHE}) as a function of the resistivity induced by the Ir impurities (ρ_{imp}). No SHE has been observed when there is no Ir impurity. With increasing the Ir impurity, however, ρ_{SHE} increases linearly with ρ_{imp}. This linear dependence clearly shows that the skew scattering is the dominant mechanism of the SHE in CuIr. From the slope of the ρ_{SHE} vs ρ_{imp} curve, it turns out that the SH angle in this system is 2.1% [1], which is consistent with the previous anomalous Hall effect measurement in CuMnIr. This SH angle is definitely larger than that obtained with pure metals [2] and indicates that scattering by impurities is a very promising way to obtain large SH angles.

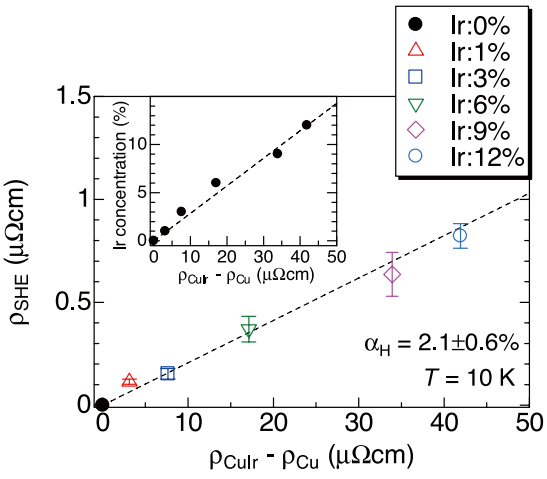

Fig. 2. Spin Hall resistivity (ρ_{SHE}) as a function of the resistivity induced by Ir impurities (ρ_{imp}) for several different concentrations. The inset shows ρ_{imp} vs Ir concentration in Cu.

References
[1] Y. Niimi, M. Morota, D. H. Wei, C. Deranlot, M. Basletic, A. Hamzic, A. Fert, and Y. Otani, Phys. Rev. Lett. **106**, 126601 (2011).
[2] M. Morota, Y. Niimi, K. Ohnishi, D. H. Wei, T. Tanaka, H. Kontani, T. Kimura, and Y. Otani, Phys. Rev. B **83**, 174405 (2011).

Authors
Y. Niimi, M. Morota, D. H. Wei, C. Deranlot[a], M. Basletic[b], A. Hamzic[b], and A. Fert[a]
[a] Unité Mixte de Physique CNRS/Thales
[b] University of Zagreb

Periodic Modulation of Local Density of States at a Ge Surface with One-Dimensional Atomic Structure

Komori Group

One-dimensional (1D) atomic structures often appear on metal adsorbed semiconductor surfaces, where we can expect interesting 1D electronic properties. We have studied local atomic and electronic structures of the Au-adsorbed Ge(001) surface with a one-dimensional chain structure in the <110> direction using scanning tunneling microscopy (STM) at 80 K. The period of the chain in the perpendicular direction is 1.6 nm, which is the quadruple length of the substrate Ge(001)-1×1 lattice constant. Figure 1(a) shows an STM image of the top of the chains at this surface. The groove between the adjacent chains is deeper than 0.3 nm, and it is difficult to observe atomic images in the grooves by STM. Previous angle-resolved photoemission spectroscopy (ARPES) studies [1,2] demonstrated a metallic surface state with the bottom binding energy about 0.15 eV below Fermi energy E_F while the direction of the strong dispersion is under debate because of the use of double domain samples in these experiments.

The top of the one-dimensional chain shown in Fig. 1(a) consists of a chevron unit of the protrusions and zigzag structures. There are characteristic combinations of the chevron unit and the zigzag structure with different lengths, which

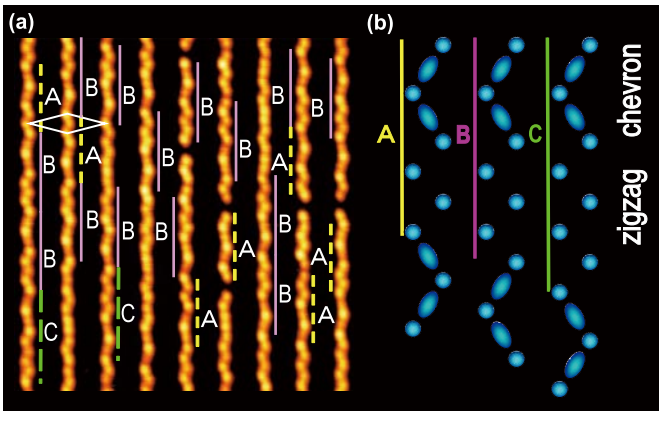

Fig. 1. (a)High-resolution topographic STM image showing protrusions on top of the chains on the surface. The image was taken at 80 K with the sample bias voltage V_b of − 1.0 V. Typical arrangements of the protrusions in the chain direction are indicated by dotted, solid and dashed lines A–C. They consist of a chevron unit and zigzag structures with different lengths. Among these arrangements, the B type is most frequently seen on the surface. The length of line B is 3.2 nm, eight times of the Ge(001) 1 × 1 lattice constant. A very local c(8×2) arrangement of the zigzag structure is indicated as the white diamond. (b) Schematic models of the three common arrangements of the protrusions consisting of a chevron unit and zigzag structures. Models A–C correspond to arrangements A–C in (a). The total length increases with increasing length of the zigzag structure.

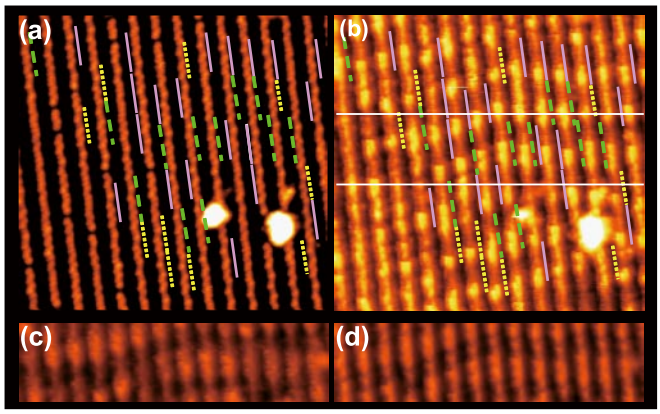

Fig. 2. (a,b) STM images of the surface showing arrangements A–C of the chain protrusions for (a) V_b = − 1.0 V and (b) V_b = − 0.2 V. Dotted, short solid and dashed lines indicate arrangements A, B and C of the chevron unit and the zigzag structure given in Fig. 1(b), respectively. (c,d) Magnified STM images of the same area as that between the two horizontal white lines in (b) for (c) V_b = + 0.1 V and (d) V_b = + 0.3 V.

are marked as the lines A-C in the figure. Schematic models of these combinations are given in Fig. 1(b). Model B occurs most frequently on the surface, and gives an eight-fold superstructure in the chain direction.

A modulation of the local density of states in the chain direction was observed by STM for a sample bias (V_b) region between − 0.2 and + 0.6 V as shown in Fig. 2(b) for V_b = − 0.2 V. Only the surface metallic band was detected by ARPES between E_F and E_F − 0.2 eV. Thus, the modulation shown in Fig. 2(b) is attributed to the metallic band. By comparing the Figs. 2(a) and 2(b), the local density of state is lower at the chevron unit than the zigzag structure for the electron energy between E_F and 0.2 eV below E_F. The local density of states is also lower at the chevron unit in the empty state as in Fig. 2(c,d). The surface metallic state has an eight-fold charge modulation in the chain direction.

References
[1] J. Schäfer, *et. al.*, Phys. Rev. Lett. **101**, 236802 (2008).
[2] K. Nakatsuji, *et. al.*, Phys. Rev. B **80**, 081406 (2009).

Authors
K. Nakatsuji, R. Niikura, and F. Komori

Reactive Rearrangements of Step Atoms by Adsorption of Tetrafluoro-tetracyanoquinodimethane on Cu(100)

Yoshinobu Group

The development of organic electronic devices such as organic light-emitting diodes, organic field-effect transistors, and photovoltaic cells requires an in-depth understanding of both electronic states and structures at organic-metal or organic-organic interfaces. In order to modify interfaces electronically, organic molecules having a strong electron affinity are expected to be useful materials for the organic electronic devices described above. In particular, tetrafluoro-tetracyanoquinodimethane (F4-TCNQ), which has a high electron affinity (EA = 5.24 eV), has been studied on various substrates from the perspective of the p-type doping of organic films, the energy-level alignment on metal surfaces, and the surface-transfer doping of semiconductor surfaces.

We investigated the local adsorption structure and

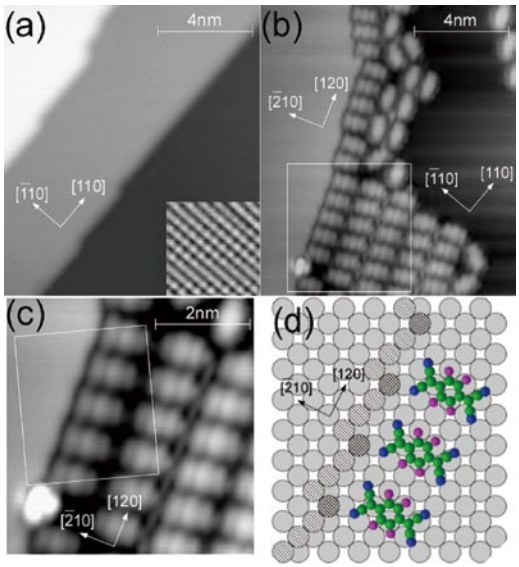

Fig. 1. (a) An STM image of the Cu(100) clean surface. The inset shows an atomic-resolution STM image of the Cu(100) terrace (2.3 × 2.3 nm^2). (b) An STM image of F4-TCNQ adsorbed at a lower step edge. (c) The close-up image of the indicated rectangle in (b). (d) A proposed structure model of F4-TCNQ adsorbed at a lower step edge (terrace Cu, gray circles; step Cu, hatched circles; kink Cu, cross-hatched circles; C, green circles; N, blue circles; F, magenta circles). The range of this structure model corresponds to the rectangle in (c). Vs and It are 0.4 V and 0.1 nA in (a), –0.2 V and 0.08 nA in (b), and 0.2 V and 0.08 nA in (c).

electronic states of F4-TCNQ on Cu(100) at low coverage using scanning tunneling microscopy (STM) and scanning tunneling spectroscopy (STS). Figure 1(a) shows a typical STM image of the clean Cu(100) surface, including a few steps. Straight steps with some kinks were usually observed. The inset in Fig. 1(a) shows an atomic-resolution STM image of the Cu(100) terrace. Based on this image, the azimuth of the Cu(100) surface was determined. It was confirmed that the direction of the step in Fig. 1(a) was mostly parallel to [110]. Figure 1(b) shows an STM image of F4-TCNQ adsorbed near a step edge. F4-TCNQ was observed as a bright elliptic protrusion. Figure 1(b) shows that F4-TCNQ molecules assemble from lower step edges. These results indicate that thermal diffusion of F4-TCNQ occurs on Cu(100) at 300 K, and F4-TCNQ prefers to adsorb at a negatively charged lower step edge. Since F4-TCNQ is a strong electron accepter, it is logical that it adsorbs at such an electron-rich site. Figure 1(c) shows a close-up STM image of Fig. 1(b). F4-TCNQ aligns with its long axis nearly perpendicular to the step edge, and the periodic kinks were observed at the step edge. The periodicity of these kinks is 0.806 nm, which agrees with the distance between F4-TCNQ molecules adsorbed at the lower step edge. Figure 1(d) shows a structure model of the F4-TCNQ species adsorbed at the lower step edge. The step edge in Fig. 1(c) is oriented at about 18.5° relative to [110]; the direction of the step edge has been changed to [120] by adsorption of F4-TCNQ, where the [120] step consists of the periodic single kinks and short step sections of 3 atom lengths. Thus, adsorbed F4-TCNQ molecules at a lower step edge induce the reactive rearrangements of Cu atoms, including the formation of periodic kinks and step etching. The cyano groups of F4-TCNQ adsorbed at the step edge interact with not only the Cu(100) terrace but also Cu atoms at an upper step edge. This extra interaction results in the asymmetric electronic states in F4-TCNQ species, which are evidenced by STM and STS [1].

Furthermore, we investigated the details of adsorption states of F4-TCNQ as a function temperature and coverage. Based on the results by photoelectron spectroscopy and vibrational spectroscopy, we found that not only charge transfer but also rehybridization occur for F4-TCNQ on Cu(100) [2].

References
[1] T. Katayama, K. Mukai, S. Yoshimoto, and J. Yoshinobu, Phys. Rev. B **83**, 153403 (2011).
[2] T. Katayama, K. Mukai, S. Yoshimoto, and J. Yoshinobu, J. Phys. Chem. Lett. **1**, 2917 (2010).

Authors
T. Katayama, K. Mukai, S. Yoshimoto, and J. Yoshinobu

Vortex Excitation in Nano-Size Superconductors by Local Current Injection

Hasegawa Group

When a type-II superconductor is subjected to an external magnetic field whose amount is larger than the lower critical field, superconductivity is locally broken and quantized amount of magnetic fluxes, or vortices, penetrate through the broken area. In the case of nano-size superconductors, however, because of the Bean-Livingston (BL) barrier existing at their periphery, vortices cannot get in even above the critical field despite a situation that being inside is energetically favorable. Here, we demonstrate that in such a "superheated" situation, a vortex can be excited into the superconductor via lowering of the barrier by a local tunneling current injected from a probe tip of a scanning tunneling microscope [1].

As a nano-size type-II superconductor, we used a Pb island structure whose thickness is ~3 nm formed on a silicon substrate. The size of the islands is ~ 100 nm, several times larger than its coherent length (31 nm at the measurement temperature (2 K)). Tunneling conductance at zero bias voltage (zero bias conductance; ZBC), that is, conductance at the bottom of a superconducting gap, provides us information on whether superconductivity below the tip is broken or not and whether a vortex is inside the superconductor or not [2]. A profile of ZBC as a function of applied magnetic field measured at the center of the island, shown in Fig. 1, exhibits a hysteresis between the vortex and Meissner (non-vortex) states, which is explained by the existence of the BL barrier.

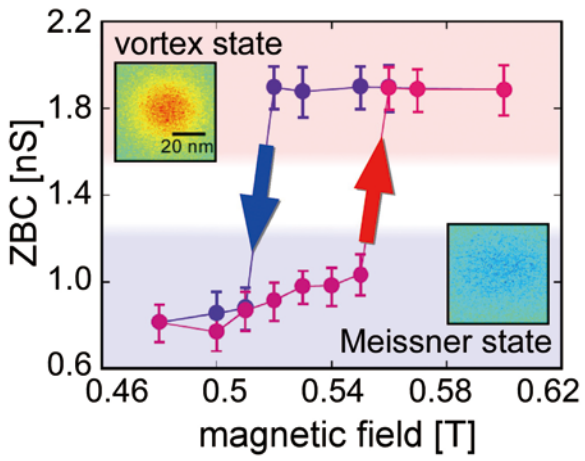

Fig. 1. Zero bias conductance as a function of applied magnetic field measured at the center of a Pb island, whose STM image is shown in Fig. 2. High (low) ZBC indicates the vortex (Meissner) states of the nano-size superconductor. Insets are ZBC images showing high (red) / low (blue) ZBC values for the corresponding two states.

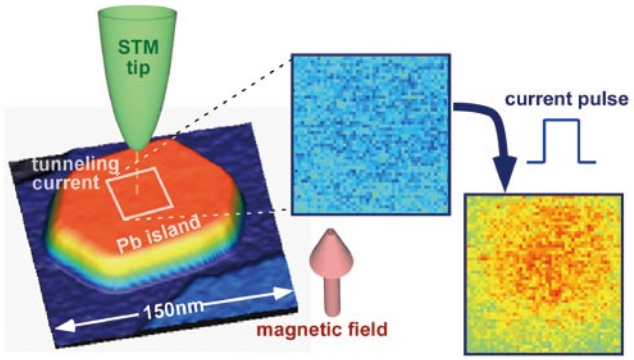

Fig. 2. Excitation of a single vortex by a pulsed current injection from an STM tip. ZBC images taken before and after the current injection indicate the vortex penetration by the pulse.

Insets in Fig. 1 are ZBC images showing high (red) / low (blue) ZBC values for the corresponding two states. A red vortex is clearly observed in the vortex state ZBC image.

We applied the magnetic field (0.55T) just below the vortex penetration field, at which ZBC jumps up, while keeping the Meissner state in order to make a metastable ("superheated") state. Then pulsed tunneling current was injected from the STM tip. ZBC images taken before and after the current injection clearly indicate vortex penetration into the Pb island during the pulse application (Fig. 2).

Repeated experiments under various conditions revealed that successful excitation needs large pulsed current (> 400 pA) and long pulse duration (> 200 ms). It is also found that current injection at peripheral sites is more preferable for the excitation than around the center of the islands. Based on calculations using a time-dependent Ginzburg-Landau equation, we conclude that the vortex excitation is induced by the formation of normal conducting area below the tip; superconductivity is locally broken first by the current exceeding the critical current density, and then once broken area is nucleated finite resistance in the area generates the Joule heat to expand the normal area. When the broken area grows large enough to lower the BL barrier, a vortex penetrates into the island. The theoretical analyses of the penetration magnetic field and its dependences on the size and site of the normal area support our experimental observations.

References
[1] T. Nishio *et al.*, Nanotechnology **21**, 465704 (2010).
[2] T. Nishio *et al.*, Phys. Rev. Lett. **101**, 167001 (2008).

Authors
T. Nishio, S. Lin[a], T. An, T. Eguchi, and Y. Hasegawa
[a]University of Tsukuba

Transport at Ruddlesden-Popper-type Interfaces

Lippmaa Group

In a quest to design and characterize quantum wells based on transition-metal oxides, it is critically important to be able to design heterointerfaces such that the physical properties of the materials forming the interface retain their bulk electronic behavior. This aim often conflicts with the crystal chemistry of many oxides. In particular, for perovskite-type interfaces, a number of processes alter the transport and magnetic behavior of the interface layers, with charge transfer, interdiffusion, and vacancy formation being some of the most important mechanisms resulting in the formation of 'dead layers' at interfaces.

In our current work[1], the aim is to explore other possible heterostructure designs that may be more robust against detrimental property changes at interfaces. Specifically, we look at one of the relatively clean oxide systems, La-doped $SrTiO_3$. When a two-dimensional layer of LaO^+ is embedded in $SrTiO_3$, metallic conductivity appears in the vicinity of the doping layer, as illustrated in Fig. 1(a). The presence of defects can be easily probed by monitoring the low-temperature carrier mobility in the system, which can reach 30,000 cm^2/Vs below 10 K. In actual La:$SrTiO_3$ delta-doping layers, the mobility is somewhat subdued, at around 3000 cm^2/Vs.

One possible choice for an interface that at least does not suffer from direct charge transfer is suggested by the Ruddlesden-Popper (RP) phases, where rocksalt layers are interleaved with perovskite blocks. As an attempt at doping a RP-type interface, we prepared heterostructures where a single (La,Sr)O atomic layer was grown on the surface of a single-crystal $SrTiO_3$ substrate and subsequently capped with a thick $SrTiO_3$ film, as illustrated in Fig. 1(b). Curiously, this structure is insulating, despite having a high density of positive charge in the (La,Sr)O rocksalt layer. Metallic conductivity in $SrTiO_3$ can be recovered by annealing the rocksalt layer before capping. By changing either the annealing temperature or time, it is possible to drive La atoms deeper into the substrate at a controlled rate. A conceptual view of the interdiffused structure, which is metallic, is shown in Fig. 1(c). The transition from insulating to metallic behavior is gradual, as illustrated by the transport data in Fig. 2.

We can identify several benefits in this type of heterostructure. Most importantly, the number of carriers is not directly controlled by the physical dopant density, since the heavily-doped rocksalt layer on its own does not contribute delocalized carriers. Since the impurity diffusion rate in a $SrTiO_3$ single crystal is low, it is easy to achieve accurate control over the electrically active dopant density, even in the range of 10^{12} cm^{-2}, which is normally hard to achieve by thin film growth techniques. By controlling the diffusion time, i.e., depth, it is also possible to control the dimensionality of the metallic layer. Since the rocksalt layers also function as

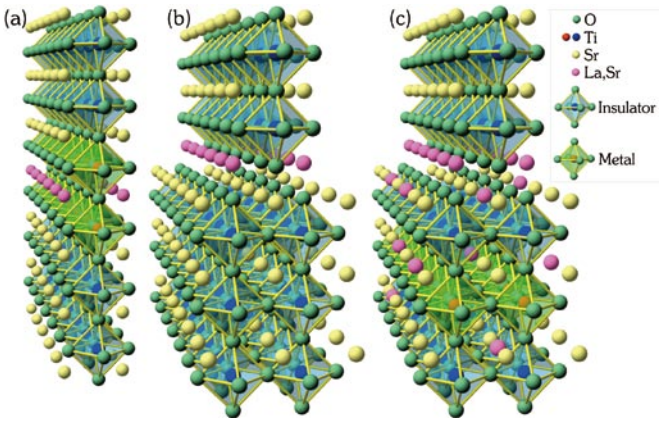

Fig. 1. Schematic diagrams of the heterostructures studied in this work: (a) a single unit cell $LaTiO_3$ layer embedded in a $SrTiO_3$ matrix, resulting in a metallic system. (b) A Ruddlesden-Popper interface, where the rocksalt layer consists of (La,Sr)O. This system is insulating, but can be made metallic by annealing (c) diffusing La atoms deeper into the substrate and forming a high-mobility metallic layer in the substrate crystal.

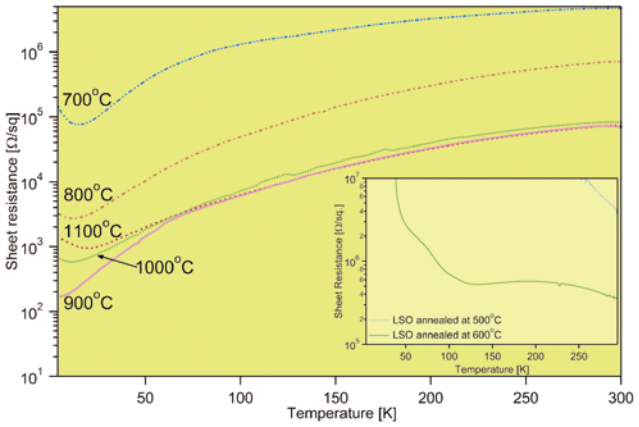

Fig. 2. Transport properties of the Ruddlesden-Popper-type heterostructures. A non-annealed interface, grown at 550 °C is insulating, while metallic conductivity gradually sets in as the annealing temperature is increased to about 900 °C. At even higher annealing temperatures other defects, mostly Sr vacancies, start to affect the low-temperature resistivity, resulting in a resistance upturn below about 20 K.

efficient diffusion barriers, it may be possible to construct well-confined quantum well structures in perovskite oxides by using two rocksalt barrier layers as the quantum well boundaries.

Reference
[1] M. Matvejeff, K. Nishio, R. Takahashi, and M. Lippmaa, Appl. Phys. Lett. **98**, 073105 (2011).

Authors
M. Matvejeff, K. Nishio, R. Takahashi, and M. Lippmaa.

Quantized Vortex Physics in hcp Solid ^{4}He and Supersolid Transition Studied by Torsional Oscillator Technique

Kubota Group

Superfluidity has been found not only in the Bose fluid, liquid ^{4}He and Fermi fluids, liquid ^{3}He and conduction electrons in metals, but also in dilute gaseous materials. Superfluidity had been considered in the early days primarily as a result of Bose Einstein Condensation (BEC) of the constituent particles, which can exchange positions with each other. The original discussions as to the possibility of observing the "supersolidity", or superfluidity in a solid were initiated in 1956 by Penrose and Onsager with a negative result, and positive discussions have gained strength in 1960's, when experimental evidence of quantized circulation, as well as quantized flux in superconductors were discovered. It was 1972 when Kosterlitz and Thouless proposed a topological two dimensional transition, describing a 2D superfluid transition at a finite temperature T_{KT}, involving 2D vortex anti-vortex pairs. Its realization was experimentally clearly shown by the study of a superfluid transition in a monolayer of He by Bishop and Reppy. We have been studying a series of artificial 3D superfluids in monolayers of He condensed on well controlled, porous glass substrates with fixed diameters [1]. We could show 3D vortex excitations in such a system both by theory [2] and experiments [3].

Here we report on our recent quantized vortex physics in

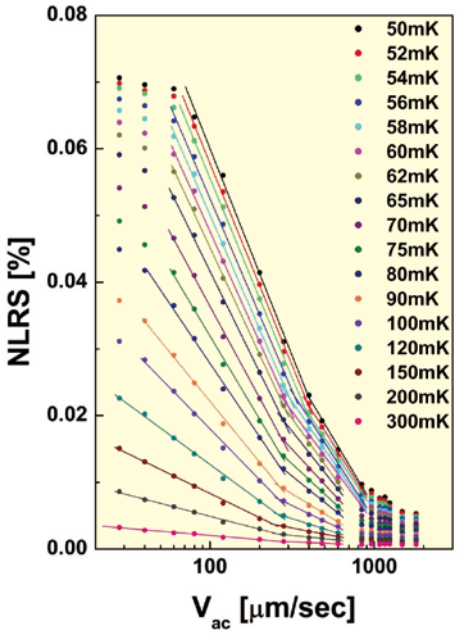

Fig. 1. Detailed measurements of the non linear rotational susceptibility, *NLRS* of our 49 bar sample of hcp ^{4}He, as a function of log *Vac* , a part of which has been published [4]. A much more detailed study is shown here. We observe the log*Vac* linear relation is followed over some range of *Vac*, starting at a certain *Vac* value. Then some other log *Vac* linear like dependence appears at a higher *Vac* range for each point at a *T*. Expanded details are discussed separately. And the turning points are plotted in Fig. 2., where a jump was found near T_c. The log *Vac* linear relation was discussed for solid ^{4}He first by Anderson [5] as evidence for the involvement of quantized vortex lines in the physics of solid ^{4}He, and is experimentally discussed by Penzev et al. [4] for vortex lines threading into or "polarizing" a tangled state of the VF.

hcp solid ^{4}He studied by detailed measurements of torsional oscillator responses under AC and DC rotation and evidence of the new features of the supersolid state as well as the quantized vortex state in this quantum solid, while quite a large number of people still try to understand the reported properties without involvement of quantized vortices or superfluidity in the solid, but by discussing classical responses of dislocations or glassy properties of the solid.

Our publication [4] discussed the onset of the vortex fluid (VF) state [5], pointing out the sudden start of non-linear response of the torsional oscillator (TO) with hcp ^{4}He samples in response to delicate change of the drive velocity V_{ac}. We discussed also the logV_{ac} linear decrease of the non linear rotational susceptibility, *NLRS* and its temperature, *T* dependent change, as the evidence of the VF state [4].

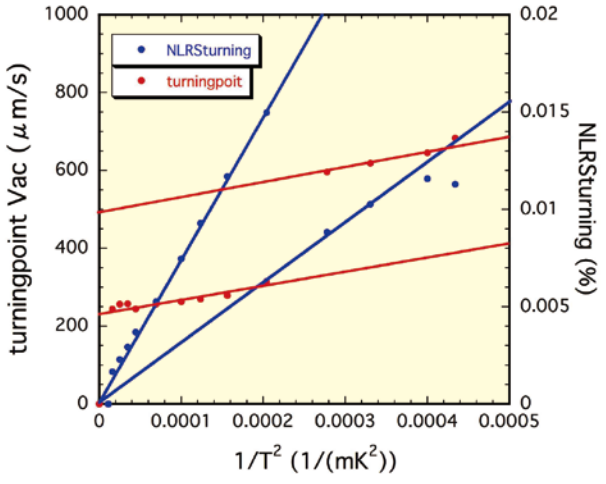

Fig. 2. The turning V_{ac} points, as well as, corresponding *NLRS* points are plotted as a function of $1/T^2$.

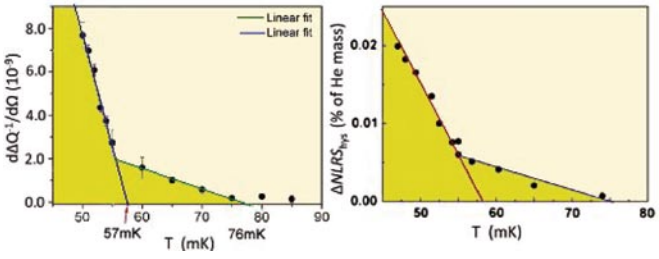

Fig. 3. The extra energy dissipation under DC rotation divided by rotational speed Ω would give a normalized energy dissipation per unit of vortex line density (left). It gives a unique T dependence and is compared with the hysteretic component of the TO response (right). It supports the idea that the hysteretic component of $NLRS_{hys}$ as the order parameter of the SS state, and probably is proportional to or is just the supersolid density ρ_{ss}.

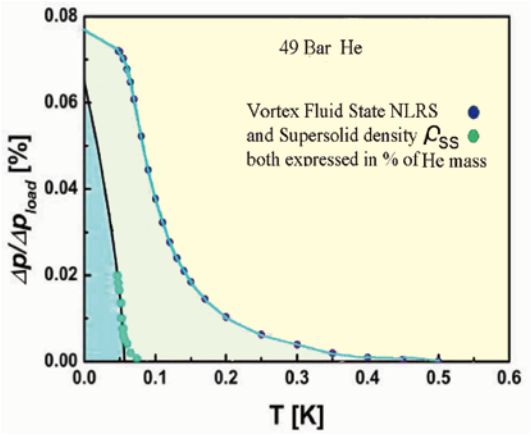

Fig. 4. Proposed Supersolid density ρ_{ss} of the SS state as well as $NLRS$ ($V_{ac}\rightarrow 0$) in the VF state in unit of % of the total solid He mass as a function of T. The transition to the SS state is sudden as seen in Fig.3 and the VF state starts gradually with $1/T^2$ dependence, but below T_o.

Further detailed analysis [6] displayed in Fig. 1 indicates a peculiar change of the logV_{ac} linear slope at a certain V_{ac} value for a specific T. The turning V_{ac} points as well as corresponding $NLRS$ points are plotted in Fig. 2 as a function of $1/T^2$. We observe a jump between $1/T^2$ ~2 and ~3 $\times 10^{-4}$ K^{-2}, for temperatures in the range ~58 mK and ~71 mK, which coincides with our earlier report [7] of the appearance of a hysteretic component below T_c ~ 75 mK (see Fig. 3) and the proposal of the order parameter of the supersolid state [7].

The macroscopic coherence of the supersolid(SS) state is probably revealed below the same T_c, by our TO response study[8] of the vortex lines penetration under DC rotation. Its data are inter-compared with the hysteretic component T dependence in Fig. 3. And we display the hysteretic component of the SS state and the VF state $NLRS$ ($V_{ac}\rightarrow 0$) in Fig. 4 [6] in the unit of % of the solid He total mass, proposing that $NLRS_{hys}$ is actually the supersolid density ρ_{ss} itself. These TO experiments have been performed using a supreme rotating cryostat built by Kubota group [9].

References

[1] M. Kubota, Surf. Sci. **283**, 404 (1993).
[2] T. Obata and M. Kubota, Phys. Rev. B **66**, 140506(R) (2002).
[3] M. Fukuda, M. K. Zalalutdinov, V. Kovacik, T. Minoguchi, T. Obata, M. Kubota, and E. B. Sonin, Phys. Rev. B **71**, 212502 (2005).
[4] A. Penzev, Y. Yasuta, and M. Kubota, Phys. Rev. Lett. **101**, 065301 (2008).
[5] P. W. Anderson, Nature Physics **3**, 160 (2007).
[6] M. Kubota, N. Shimizu, Y. Yasuta, A. Kitamura, and M. Yagi, J. Low Temp. Phys. **162**, 483 (2011).
[7] N. Shimizu, Y. Yasuta, and M. Kubota, arXiv:0903.1326.
[8] M. Yagi, A. Kitamura, N. Shimizu, Y. Yasuta, and M. Kubota, J. Low Temp. Phys. **162**, 492 (2011).
[9] M. Yagi, A. Kitamura, N. Shimizu, Y. Yasuta, and M. Kubota, J. Low Temp. Phys. **162**, 754 (2011).

Authors
M. Kubota, N. Shimizu, Y. Yasuta, A. Kitamura[a], and M. Yagi
[a]Niigata University

Quantum Hall Transport in Graphene Junctions

Osada Group

The electronic system of graphene can be regarded as a two-dimensional massless Dirac fermion system in solids resulting in remarkable relativistic behaviors. For example, carriers in graphene can never be confined by any potential barriers because of the Klein tunneling property. So, it is expected that graphene junctions, where two graphene systems under different potential touch with each other, show characteristic transport properties. In fact, the quantum Hall transport across the p-n bipolar junction of monolayer graphene have attracted much attention because of its fractional quantization of two-terminal conductance.

We have studied the quantum Hall transport of two other graphene junctions, the monolayer-bilayer hetero-junctions and the p-n bipolar junctions of bilayer graphene, for the first time (Fig. 1). In the quantum Hall state, two regions in both sides of the junctions have different quantum Hall indices (Chern numbers). Therefore, there should exist metallic states along the boundary between these regions. The purpose of research is to clarify the contribution of these boundary states to the quantum Hall transport.

The monolayer-bilayer graphene heterojunctions are interesting systems because of its pseudo-spin selectivity. To study quantum Hall transport in this system, we have used junctions formed accidentally in mechanical exfoliation on SiO_2/n-Si substrate, which works as a gate electrode. As a function of gate voltage, the two-probe conductance across the monolayer-bilayer boundary shows the "V"-shaped characteristics with the staircase-like modulation corresponding to the Shubnikov-de Haas effect in both regions (Fig. 2). The plateau heights of the staircase seem to almost coincides with fractional multiple of e^2/h. This result has been considered using the Landauer-Buttiker formalism of edge channel transport in the quantum Hall state, which was also applied to the p-n junction of monolayer graphene. The observed result can be well explained by assuming full-mixing of edge states at the monolayer-bilayer boundary. This means that carriers in any input edge channels are distributed to all output channels with equal transmission

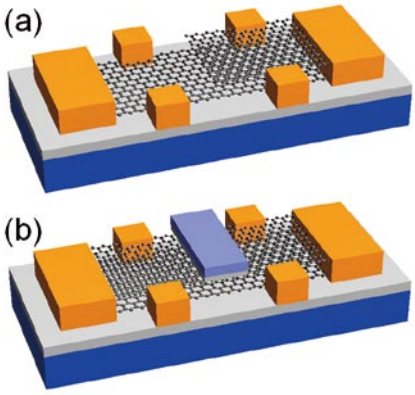

Fig. 1. (a) Monolayer-bilayer heterojunction device of graphene. (b) p-n-p double bipolar junction device of bilayer graphene.

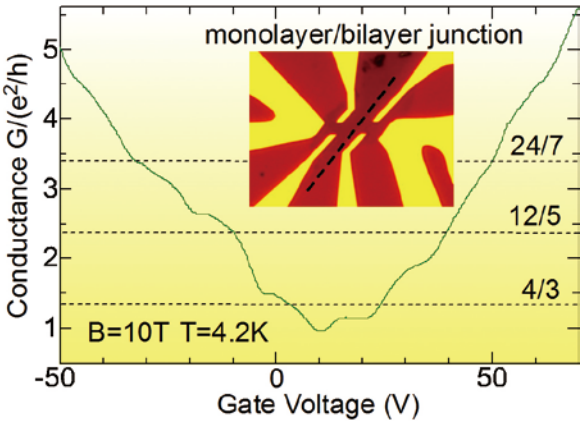

Fig. 2. Gate voltage dependence of two-terminal conductance of the monolayer-bilayer hetero-junction device of graphene. Dotted lines indicate the plateau heights predicted by Landauer-Buttiker picture assuming full-mixing of edge states.

probability.

Bilayer graphene is promising for device application because its energy gap can be controlled by external electric fields. The p-n bipolar junctions of bilayer graphene can be realized by the FET structure with an additional top gate electrode covering the sample partially. In this case, the top gate voltage does not only changes the potential of the gated region, but also opens the energy gap in the gated region. In the quantum Hall state, this energy gap breaks the degeneracy of the n=0 Landau level causing the n=0 quantum Hall plateau forbidden in the zerogap case. Therefore, we can expect interplay of quantum Hall transport and opening of the energy gap (namely, appearance of the n=0 quantum Hall state) in the partially gated bilayer. We have measured the two-terminal resistance of p-n-p double junctions of bilayer graphene as a function of top- and back-gate voltage. The resistance plateaus exhibit diamond-like pattern on the top- and back-gate voltage plane similar to that observed in p-n junctions of monolayer. The remarkable difference is the existence of high resistance regions along the charge neutral line of the top-gated region at high gate voltages. It corresponds to the appearance of the n=0 quantum Hall state. The observed plateau values can be almost explained by Landauer-Buttiker picture assuming full mixing of edge states along the p-n junction.

Authors
T. Osada, A. Tsukuda, H. Okunaga, K. Uchida, and T. Konoike

Pressure-induced Superconductivity and Valence Change on $EuFe_2As_2$

Uwatoko, Y. Ueda and Ohgushi Groups

In the oxygen-free iron arsenide AFe_2As_2 (A = Ca, Sr, Ba, Eu) with the FeAs layers tetragonal $ThCr_2Si_2$ structure, the antiferromagnetism of Fe moments is suppressed by chemical doping or applying pressure, and superconductivity appears above a critical concentration and pressure. Among the AFe_2As_2 compounds, $EuFe_2As_2$ offers an unique opportunity to study an interplay between the superconductivity and magnetism of both Eu and Fe ions [1,2]. As for the competition between the superconductivity and magnetism of Eu ions, it would be also rewarding to extend the pressure

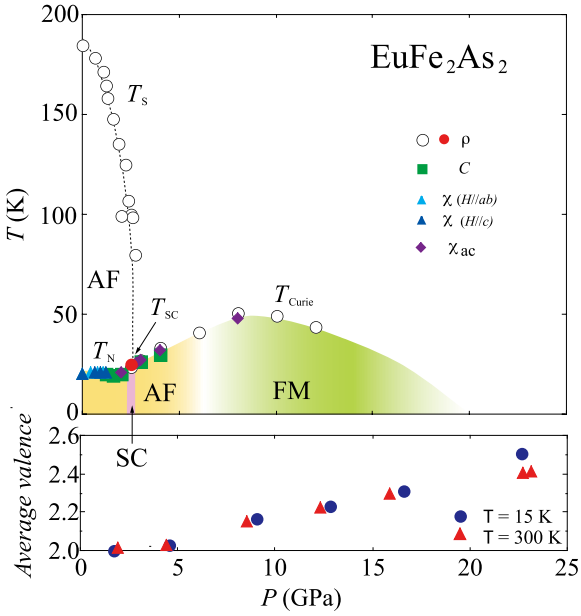

Fig. 1. Pressure-temperature phase diagram of $EuFe_2As_2$ derived from the electrical resistivity (open and closed circles), ac specific heat (squares), and magnetic susceptibility (triangles and diamonds). The lower-panel shows the pressure dependence of the averaged valence.

range to higher pressure because sufficiently high pressure induces the valence change from Eu^{2+} ($4f^7$, magnetic) to Eu^{3+} ($4f^6$, non-magnetic) state, which may be more favorable for the appearance of superconductivity. In order to clarify these points and construct the phase diagram in the wider pressure range, we have measured electrical resistivity, ac specific heat, magnetic susceptibility, X-ray absorption spectroscopy (XAS) and X-ray magnetic circular dichroism (XMCD) of the $EuFe_2As_2$ single crystal grown by the self-flux method up to 23 GPa.

Figure 1 shows the pressure-temperature phase diagram of $EuFe_2As_2$. The antiferromagnetism associated with Fe moments is suppressed at P_C ~ 2.5-2.7 GPa while the antiferromagnetic order of localized Eu moments is almost pressure independent below P_C. Our key finding is that T_{SC} only appears in the narrow pressure region in the vicinity of P_C, indicating that the SC state competes with the AF state of Eu^{2+} moments. Above 3 GPa, T_N of Eu^{2+} moments starts to increase, and a pressure-induced transition from antiferromagnetic to ferromagnetic ordering is confirmed by the ac magnetic susceptibility and ESM measurements. The magnetic coupling between the Eu moments would be mediated by the indirect Ruderman-Kittel-Kasuya-Yosida (RKKY) exchange interaction in $EuFe_2As_2$. It is conceivable that the RKKY exchange interaction could be affected by the distance between Eu moments with applying pressure, resulting in the pressure-induced variation from antiferromagnetic to ferromagnetic order due to the sign change of the RKKY interaction. It is found that the ferromagnetic transition temperature T_{Curie} shows a maximum at around 8 GPa, and decreases at higher pressures. Combining the results of XAS and XMCD data, the suppression of the ferromagnetic state is connected with the valence change from magnetic Eu^{2+} to nonmagnetic Eu^{3+} state. According to the recent the x-ray diffraction measurement under pressure in $EuFe_2As_2$, collapsed tetragonal (cT) phase is found above 8 GPa [3]. It is known that the pressure- induced structural transition toward the cT phase is connected with the valence change of Eu ions, as reported in $EuFe_2P_2$ and $EuCo_2P_2$ [4]. Therefore, we conclude that pressure-induced valence change occurs at ~ 8 GPa.

References
[1] C. F. Miclea, M. Nicklas, H. S. Jeevan, D. Kasinathan, Z. Hossain, H. Rosner, P. Gegenwart, C. Geibel, and F. Steglich, Phys. Rev. B **79**, 212509 (2009)
[2] T. Terashima, M. Kimata, H. Satsukawa, A. Harada, K. Hazama, S. Uji, H. S. Suzuki, T. Matsumoto, and K. Murata, J. Phys. Soc. Jpn. **78**, 08370 (2009)
[3] W. Uhoya, G. Tsoi, Y. K. Vohra, M. A. McGuire, A. S. Sefat, B. C. Sales, D. Mandrus, and S. T. Weir, J. Phys.: Condens. Matter **22**, 292202 (2010).
[4] B. Ni, M. M. Abd-Elmeguid, H. Micklitz, J. P. Sanchez, P. Vulliet, and D. Johrendt, Phys. Rev. B **63**, 100102 (2001).

Authors
K. Matsubayashi, K. Munakata, N. Katayama, M. Isobe, K. Ohgushi, Y. Ueda, N. Kawamura[a], M. Mizumaki[a], N. Ishimatsu[b], M. Hedo[c], I. Umehara[d], and Y. Uwatoko
[a]JASRI/SPring-8
[b]Hiroshima University
[c]University of the Ryukyus
[d]Yokohama National University

Ultrafast Coherent Control of Spin Precession Motion by Terahertz Magnetic Pulses

Suemoto Group

Ultrafast optical coherent control of the spin degrees of freedom is currently receiving intense attention. Preceding reports on demonstrations of coherently controlling the spin systems have been conducted using indirect excitations of the spins that occur as a result of dielectric interaction with optical pulses such as electronic excitations and inverse Faraday effect. Detecting methods of the spin precessions in these studies are generally also indirect and monitor the spins through fluctuation of dielectric constants. Very recently, we succeeded to show that spin precessions are directly excited by magnetic field of a terahertz pulse and observed in time domain via terahertz (THz) emission with a circular polarization from the spin system [1]. In this report, we will demonstrate coherent control of spin precession motions in canted antiferromagnet $YFeO_3$ by the double pulse excitation technique using impulsive magnetic fields [2].

As shown in Fig.1, the magnetic moment experiences a force which equals to the cross product of the magnetic moment and the impulsive magnetic field (H_{THz}) by a first pulse, and is tilted. After this tipping, the magnetic moment starts to precess around the effective magnetic field in the z-axis direction (Fig. 1(a)). The induced precessions of the spins are expected to radiate free induction decay (FID) signal as a circularly polarized electromagnetic wave with a

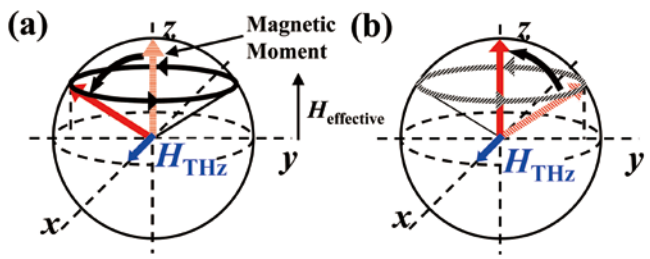

Fig. 1. Illustration showing the dynamics of magnetic moment. (a) The magnetic moment is tilted within y-z plane by the impulsive magnetic field by the first pulse along x-axis (blue arrow), and begins precession motion around z-axis. (b) Inserting the second magnetic pulse, the precession of the magnetic moment stops and the moment is directed along z-axis.

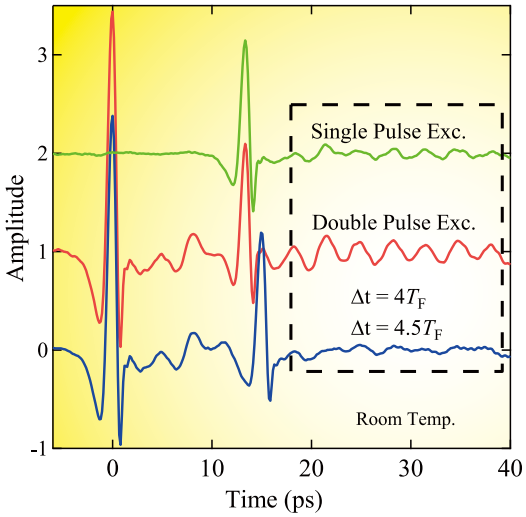

Fig. 2. Temporal waveforms of transmitted THz wave through c-cut plane parallel plate of $YFeO_3$ for single (green curve) and double pulse (red and blue curves) excitation. The waveforms consist of the half-cycle THz main pulse and oscillation components which reflect the spin precession motion.

frequency equal to the precession frequency, which persists within the transverse relaxation time. Furthermore, inserting the second magnetic pulse with the appropriate time interval as shown in Fig.1(b), the rotated magnetic moment stops and the moment is directed along z-axis. The magnetic component of the THz pulse with a half-cycled waveform can be regarded as an ultrashort magnetic pulse with the pulse duration of ~ 0.3 ps. We can probe the motion of the magnetic moment by observing the THz emission from the magnetic moment.

Figure 2 shows the experimental result of THz waveforms transmitted through the sample with single and double pulse excitations. The waveforms consist of the half-cycle THz main pulse and oscillation components by the spin precessions due to the ferromagnetic resonance (the oscillation period is T_F ~ 3.3 ps or the frequency is 0.299 THz). The oscillation decays by the FID radiation and other relaxation processes within the condensed matter. The oscillation amplitude after the second main pulse for double pulse excitation is enhanced at $\Delta t = 4T_F$ (red curve). On the other hand, the oscillation amplitude for $\Delta t = 4.5T_F$ (blue curve) are cancelled perfectly. These facts indicate that we succeeded in the coherent control of the spin precession by the ultrashort magnetic pulses and the amplitude can be controlled by the time interval of the THz magnetic pulses. In the case of $\Delta t = 4T_F$, the amplitude is increased twice, i.e., the stored energy of the spin precession is four times larger. In the case of $\Delta t = 4.5T_F$, the amplitude becomes zero and the energy of the spin system given by the first pulse is transferred back to the second THz pulse.

We demonstrated the ultrafast coherent control of spin precession motion by the impulsive magnetic field for the first time. This technique opens up the possibility of new application for the spin control in the field of quantum information and spintronics, because the effective usage of THz magnetic pulses enables us to observe directly the response of the magnetic dipole transition and to control the spin system with several orders lower energy compared to that in the preceding studies using optical pulses.

References
[1] M. Nakajima, A. Namai, S. Ohkoshi, and T. Suemoto, Opt. Exp. **18**, 18260 (2010).
[2] K. Yamaguchi, M. Nakajima, and T. Suemoto, Phys. Rev. Lett. **105**, 237201 (2010).

Authors
M. Nakajima, K. Yamaguchi, and T. Suemoto

Electron Beam Induced Disordering of a Surface Structure at Low Temperatures

Takahashi Group

Ground state of low-dimensional materials is often characterized by electron-lattice interaction and electron-electron interaction, since these interactions become more important in reduced dimensions. The $\sqrt{3}\times\sqrt{3}$ triangular array of Sn atoms on the Ge(111) surface has been widely studied in surface science as a good touchstone of such low-dimensional characteristics. The electron-lattice interaction drives the rearrangement of the Sn atoms, one-third Sn atoms are placed at a higher position and the rest two-thirds ones at a lower position [see Fig. 1(b)], accompanied by the electron transfer from the down atoms to the up ones. Recently, the 1-up and 2-down (1U2D) distribution of the Sn atoms was reported to change into the flat one below 30 K, accompanied by the gap-opening of a metallic surface state band [1]. The gap-opening was attributed to the strong electron correlation in the half-filled narrow-width surface state band, and the new phase was considered as a tow-dimensional Mott insulator. The newly found phase transition had been inspected by other groups, but consensus was not reached on the nature of the ground state.

We show in this report that the reported flat arrangement of Sn atoms is an artifact, which is cause by external stimuli of surface probes. We found that the 1U2D arrangement can be destructed by low-energy (~50 eV) electron beam only below ~30 K [2]. The electron beam effect was confirmed as follows. We cooled the sample down to 14 K without the electron beam irradiation, and then started the irradiation with the observation of its diffraction pattern at 14 K. At the beginning of the irradiation, the surface showed clear diffraction spots specific to the 1U2D structure, however, the diffraction spots became weak and broad with the irradiation time. After the measurement we changed the sample position to a non-irradiated area and observed clear 1U2D spots. The 1U2D spots decayed with irradiation time in the way. Therefore, the disordering of the 1U2D arrangement is caused by the electron beam, and the 1U2D arrangement remains even below 30 K if the surface is untouched. Other diffraction spots which come mainly from the in-plane arrangement of Sn atoms did not changed, indicting that the 1U2D height distribution of Sn atoms is disordered by electron beam. Fig. 1(a) shows current density dependence of the diffraction amplitude attenuation. The initial slope of the amplitude decrease became steeper with the current density. Estimated rate of amplitude attenuation depends on the current density linearly, indicating that the vertical arrangement change is caused by a single electron. The cross section for the structure change, estimated from the rate of diffraction amplitude decrease, is comparable to that of electronic excitation of valence bands. Since the charge transfer between the up and down Sn atoms is strongly correlated with the vertical motion of Sn atoms, it is suggested the incident electrons cause the vertical motion through the electronic excitation and disorder the 1U2D height arrangement. Fig. 1(c) shows temperature dependence of the electron beam effect. The artificial structure change did not occur above ~40 K and became significant below ~30 K, indicating that a temperature dependent nature makes the surface sensitive to the structure change as seen in a semiconductor surface which has the similar electron-lattice coupling properties [3].

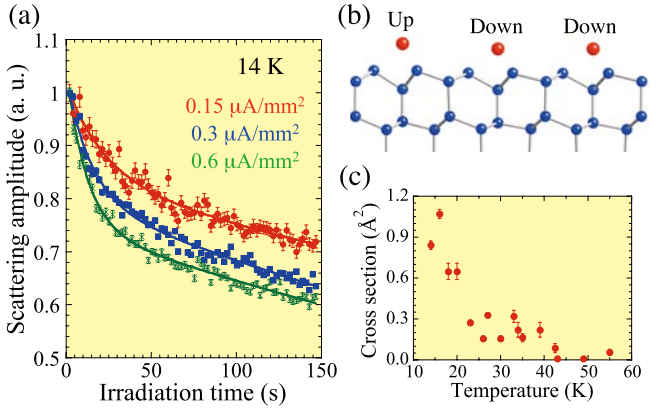

Fig. 1. (a) Current density dependence of the electron beam effect at 14 K. Scattering amplitudes of the electron diffraction spot specific to the 1U2D structure are plotted with respect to the irradiation time. Electron energy is 50 eV. (b) The 1U2D structure of the Sn/Ge(111) surface. (c) Temperature dependence of the cross section for the structure change for a 50-eV electron.

References
[1] R. Cortes *et al*., Phys. Rev. Lett. **96**, 126103 (2006).
[2] T. Shirasawa, H. Tochihara, K. Kubo, W. Voegeli, and T. Takahashi, Phys. Rev. B **81**, 081409(R) (2010).
[3] T. Shirasawa, S. Mizuno, and H. Tochihara, Phys. Rev. Lett. **94**, 195502 (2005).

Authors
T. Shirasawa, H. Tochihara[a], K. Kubo, W. Voegeli, and T. Takahashi
[a]Kyushu University

Development of an *in situ* Surface Magneto-Transport Measurement System with Multi-Probes and Observation of Enhanced Spin Relaxation in a Ultrathin Metal Film by the Rashba-Type Surface

I. Matsuda Group

Nowadays, there has been growing interests in materials of the nanometer/atomic-scale that are synthesized by

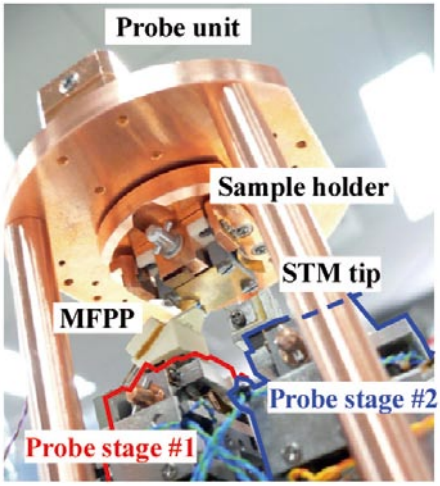

Fig. 1. A photograph of the independently-driven double probe stages, equipped with a Micro-Four-Point Probe (MFPP) and a STM tip.

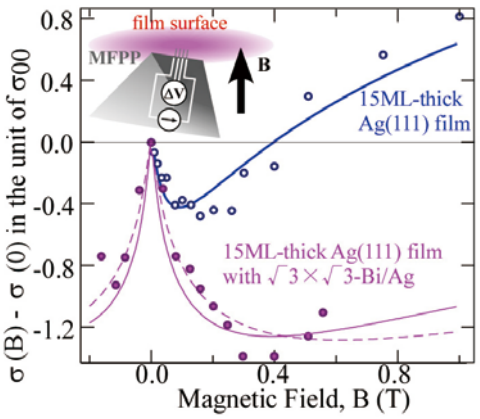

Fig. 2. Magneto-conductance data for the bare (blue open circles) and $\sqrt{3}\times\sqrt{3}$- Bi/Ag-terminated (purple solid circles) 3.5nm-thick Ag(111) film. Solid and broken lines are fits to the data according to the HLN formula. Two possible curve-fits were performed for the Bi/Ag(111) film with the different fitting parameters. σ_{00} is the quantum unit of conductance.

self-organizations on solid surfaces, typically in ultrahigh vacuum (UHV). Transport measurements on such fine structures have inevitably required the surface-sensitive probes and, recently, so-called the micro-four-point-probe (MFPP) method has been developed. This is the four-point probe method with the probe-spacing of micrometers so that the probing current flows only near the surface region. The measurements have been performed using monolithic MFPP or independently driven four-tip scanning tunneling microscope (STM) probes. Conductance of various nanofilms and surface superstructures on semiconductor substrates have been reported by the technique. On the other hand, the surface transport researches have lacked measurements under magnetic field that provide information, for example, on the carrier-type and the carrier-density (the Hall effect) or on the phases of the conducting electrons (the weak localization effect). Only a few attempts have been so far made on such *in situ* measurements, mainly due to the experimental difficulty.

In the present work, we have developed an independently-driven double probe-stage system for *in situ* magneto-transport measurements for surface systems (Fig. 1). The measurement can be performed at low temperature down to 7.6 K, with magnetic field up to 7 T under ultrahigh vacuum condition below 1×10^{-8} Pa. Various types of probes, i.e. a monolithic MFPP or an STM tip, can be mounted on the probe-stage.

Then, we have performed magneto-conductance measurements on bare and $(\sqrt{3}\times\sqrt{3})$-Bi/Ag-covered ultrathin

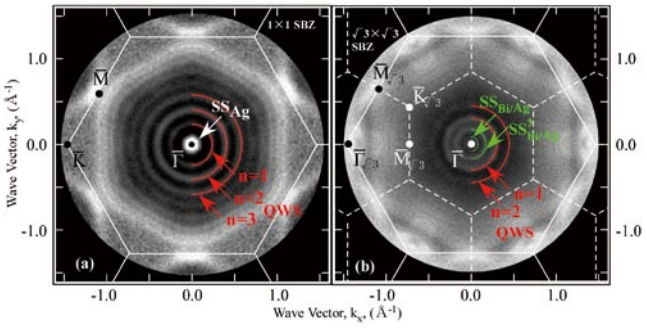

Fig. 3. Photoemission Fermi surfaces for (a) bare and (b) $\sqrt{3}\times\sqrt{3}$-Bi/Ag-terminated 3.5nm-thick Ag(111) films measured at hν =49.6 eV. The 1×1 and $\sqrt{3}\times\sqrt{3}$ surface Brillouin zones, along with their symmetry points, are also shown as solid and broken lines, respectively. Lines are used to mark the energy contours of quantum-well states and surface states.

(3.5nm-thick) Ag(111) films by the micro-four-point probe (MFPP) method. For both systems, we detect weak localization and weak anti-localization effects, with significantly different magnetic field dependence in the two cases (Fig. 2). The experimental curves were analyzed by introducing the results of photoemission investigation (Fig. 3) and band structure calculations into the Hikami-Larkin-Nagaoka (HLN) formula, in order to derive the characteristic fields of the two systems. The formation of the Rashba-type surface alloy was found to reduce the spin relaxation time in the ultrathin film significantly, without affecting the phase coherence time.

References

[1] N. Miyata, R. Hobara, H. Narita, T. Hirahara, S. Hasegawa, and I. Matsuda, Jpn. J. Appl. Phys. **50**, 036602 (2011).

[2] N. Miyata, H. Narita, M. Ogawa, A. Harasawa, R. Hobara, T. Hirahara, P. Moras, D. Topwal, C. Carbone, S. Hasegawa, and I. Matsuda, Phys. Rev. B **83**, 195305 (2011).

Authors

N. Miyata, H. Narita, M. Ogawa, A. Harasawa, R. Hobara, T. Hirahara, P. Moras[a], D. Topwal[b], C. Carbone[a], S. Hasegawa, and I. Matsuda

[a]Istituto di Struttura della Materia, Consiglio Nazionale delle Ricerche

[b]International Centre for Theoretical Physics (ICTP)

Peierls Mechanism of the Metal-Insulator Transition in Ferromagnetic Hollandite $K_2Cr_8O_{16}$

Y. Ueda Group

Metal-insulator (MI) transition is one of the most drastic phenomena in strongly correlated electron systems. The chromium hollandite, $K_2Cr_8O_{16}$ is quite unique not only in its rare mixed valence of Cr^{3+}/Cr^{4+} but also in its MI transition; it has a metal (or half-metal) to insulator transition in a ferromagnetic state and the resulting low temperature phase is a rare case of a ferromagnetic insulator (FI) [1].

X-ray diffraction experiments for the single crystal using synchrotron radiation source have revealed the structure change from a tetragonal $I4/m$ structure of the ferromagnetic metal (FM) phase to a monoclinic $P112_1/a$ (or $P112_1/b$) structure of the FI phase [2]. This structural change is accompanied by the loss of four-fold symmetry and mirror plane perpendicular to the c-axis, and furthermore the unit cell becomes large as $\sqrt{2}a \times \sqrt{2}b \times c$, where a, b and c are the lattice parameters in the FM phase. In the FI phase, four Cr sites (Cr1 - Cr4), two K sites (K1 and K2) and eight oxygen sites (O1 - O8) become crystallographically inequivalent, as shown in Fig. 1, in contrast to unique Cr and K site and two O sites in the FM phase. Although there are distinct four Cr sites (Cr1 - Cr4), the average values of the Cr-O bond lengths for four Cr sites are almost the same and the Cr valences estimated via the bond valence sum are the same within the experimental errors, indicating the absence of charge separation and order. Instead, the characteristic Cr-O bond alternations along the c-axis are observed in the rectangular column formed by four CrO_6 ($Cr1O_6$ - $Cr4O_6$) chains. Such bond alternations indicate a mass of four Cr ions (tetramer) in the four-chain rectangular columns. These observed structural characteristics well coincide with a Peierls mechanism for the MI transition from band calculation [2]; $K_2Cr_8O_{16}$ with the averaged valence of $Cr^{3.75+}$ has one extra electron per

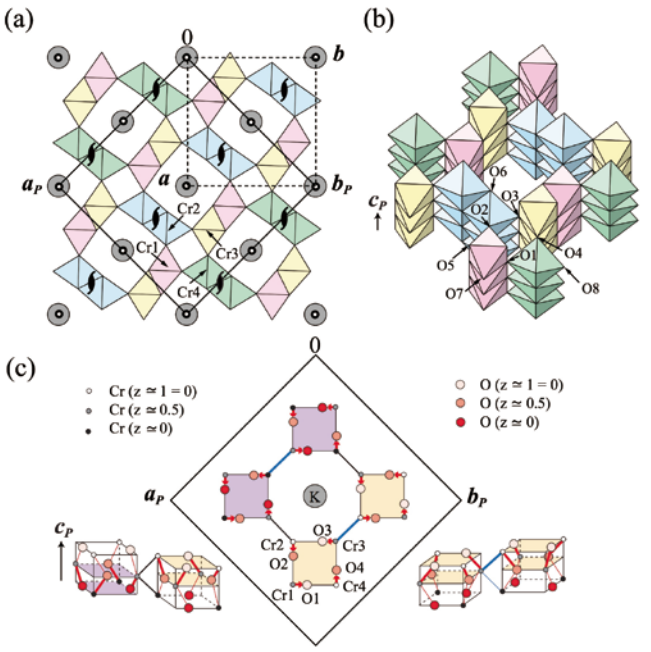

Fig. 1. (a) Crystal structure of $K_2Cr_8O_{16}$ at 20 K viewed from the *c*-axis. The unit cells of the FM phase (dotted lines) and the FI phase (solid lines) are shown. Inversion centers and two-fold screw axes are indicated by open circles and solid symbols, respectively. (b) Part of the crystal structure showing connection of the double Cr chains running along the *c*-axis. (c) Schematic illustration of the FI phase. Thicker lines represent shorter Cr-O or Cr-Cr bonds. The four-chain rectangular columns with up/down tetramerization are arranged in the stripe-like pattern.

four Cr ions on top of the valence $Cr^{4+}$and one extra electron is weakly localized in the Cr1 - Cr4 tetramer due to Peierls instability inherent in one dimensional electron system characterized by the four-chain rectangular column. The spatial arrangement of the four-chain rectangular columns with the tetramers has neither uniform type nor checkerboard type, but it has an unexpected stripe type, as shown in Fig. 1(c). Such a stripe type arrangement could result from the competition between ferro-arrangement due to lattice distortion and antiferro-arrangement due to coulomb repulsion.

References

[1] K. Hasegawa, M. Isobe, T. Yamauchi, H. Ueda, J-I. Yamaura, H. Gotou, T. Yagi, H. Sato, and Y. Ueda, Phys. Rev. Lett. **103**, 146403 (2009).

[2] T. Toriyama, A. Nakao, Y. Yamaki, H. Nakao, Y. Murakami, K. Hasegawa, M. Isobe, Y. Ueda, A. V. Ushakov, D. I. Khomskii, S. V. Streltsov, T. Konishi, and Y. Ohta, submitted to Phys. Rev. Lett.

Authors

Y. Ueda, M. Isobe, A. Nakao[a], H. Nakao[a], Y. Murakami[a], T. Konishi[b], and Y. Ohta[b]

[a]KEK

[b]Chiba University

Finite-temperature Phase Transition to the *m*=1/2 Plateau Phase in the Spin-1/2 XXZ Model on the Shastry-Sutherland Lattices

Kawashima Group

Fractional magnetic plateaus have been observed at a very low temperature in recent experiments on several rare-earth metal compounds RB_4. The trivalent ions R^{3+} in the *ab*-plane form the Shastry-Sutherland lattice (SSL). In TmB_4, an extended magnetization plateau at m=1/2 was confirmed for H_{c1}~1.9 T < H < H_{c2} = 3.6 T when magnetic fields were applied along the *c* axis [1]. Here, m is the magnetization value normalized by the saturation magnetization. In contrast to the well-known SSL compound $SrCu(BO_3)_2$, TmB_4 has a strong easy-axis anisotropy along the *c* axis. Therefore the magnetic properties at a low temperature can be described by the S=1/2 XXZ model with easy-axis anisotropy. The most characteristic property of this effective model is that the transverse coupling is ferromagnetic, reflecting the integer magnitude of Tm^{3+} ion (J = 6). Magnetization curves for this effective model were studied by the Monte Carlo (MC) computations [2]. Authors in Ref. [2] suggested that the 1/2 plateau is stabilized when the transverse exchange coupling is finite when only J and J' are present (see Fig. 1(a)). Although the 1/2 plateau emerges by the finite transverse coupling, the 1/3 plateau always exists independently of the appearance of 1/2 plateau. In the experiments, the 1/3 plateau was not observed. Therefore the magnetization curves observed in TmB_4 were not fully understood by the short-range interaction model.

To understand the magnetic properties of this compound, we focused on the long-range interaction effect. Since this compound is a metal, it is expected that the RKKY-type interaction works between the magnetic moments. In this study, we focused on the effect of the additional couplings J_3 and J_4 shown in Fig. 1(a). The Hamiltonian is given by

$$H = J\sum_{<ij>}(S_i S_j)_\Delta + J'\sum_{<ij>'}(S_i S_j)_\Delta + J_3\sum_{<ij>''}(S_i S_j)_\Delta + J_4\sum_{<ij>'''}(S_i S_j)_\Delta ,$$

where $(\ldots)_\Delta = -\Delta(S^x_i S^x_j + S^y_i S^y_j) + S^z_i S^z_j$. In the Ising limit ($\Delta$ = 0), we can evaluate the lowest energies and, we found that the ferromagnetic J_4 couplings play a key role to stabilize the 1/2 plateau state without developing the 1/3 plateau [3].

The spin configuration of the 1/2 plateau state is characterized by the C_4 (90°-rotational) symmetry breaking around the center of the plaquette without diagonal coupling J (Fig.1

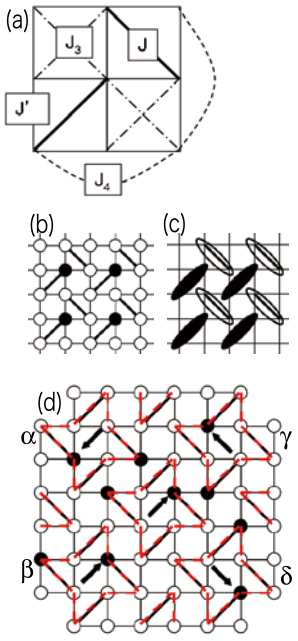

Fig. 1. (a) Effective model on the SSL. (b) and (c) are spin configurations of the 1/2 plateau in the lowest temperature phase and the intermediate phase, respectively. Up (down) spins are described by solid (open) circles and solid (open) ellipsoids are spin pairs having total S^z = 0 (1). (d) Eight-spin clusters in the 1/2 plateau phase. Spins on a closed loop form an effective clock spin. The status of the clock spin is drawn by an arrow.

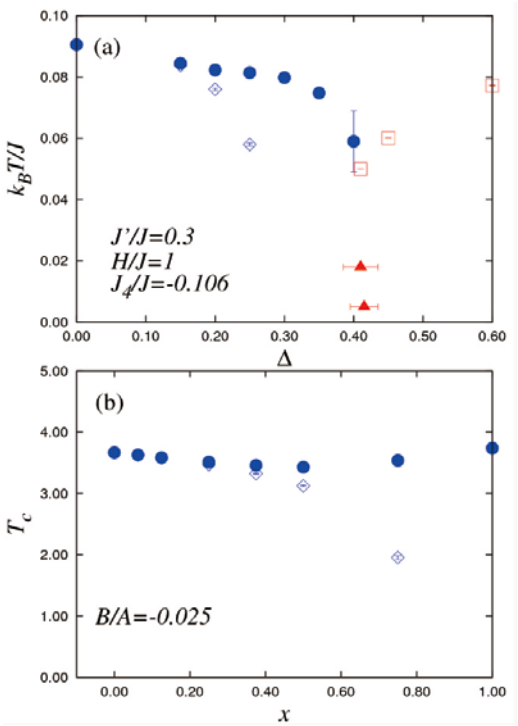

Fig. 2. (a) Δ-T phase diagram for the S=1/2 XXZ model. (b) Critical temperatures for the simplified classical model. Blue circles (diamonds) correspond to the critical temperatures. x is a coupling strength between two clock spins α and β (γ and δ) shown in Fig. 1(d). The red symbols indicate the phase boundary of the Kosterlitz-Thouless phase. The detailed definition is shown in Ref. [4].

(b)). As for the thermal phase transition associated with the C_4 symmetry breaking, there are two possible scenarios if the system shows the second-order phase transition. One is that the group C_4 breaks down to the trivial one at a single critical temperature. The other is that the system shows two-steps phase transition. In the latter case, C_2-symmetric phase realizes as the intermediate phase. The spin configuration in the intermediate phase is described by the triplet spin-pair coverings as shown in Fig. 1(c). In order to clarify the thermal phase transition, we performed the quantum MC calculation. Figure 2 (a) is the phase diagram when J'/J = 0.3, J_3/J = 0, J_4/J = –0.106, and H/J = 1. Solid circles (open diamonds) in the figure indicate that 90° (180°)-rotation symmetry breaking takes place there. In the Ising limit (Δ = 0), a single phase transition takes place. The finite-size scaling analysis for order parameters indicated that the universality class is that of the four-state Potts model [4]. When the system has the finite exchange coupling, the thermal critical properties are changed: the system shows a two-steps phase transition. To understand this difference, we proposed the simplified classical spin model, namely the generalized four-state chiral clock model [4]. The spin configurations in the Ising spin limit can be described by the arrangement of eight-spin clusters as shown in Fig. 1(d). We restrict the local Hilbert space to them and then the simplified model is obtained. By performing the classical MC computations, we investigated the thermal phase transition for the simplified model and Fig. 2(b) is the summary. The results obtained indicate that the simplified model well captures the critical properties of the original XXZ model. In Fig. 2(b), the parameter x is a quantity related to Δ. At x = 0, the simplified model is equivalent to the conventional four-state Potts model. Therefore it is trivial that the system shows a single phase transition belonging to the four-state Potts universality class. At x = 1, the energies between the spin configurations, α and β (γ and δ) in Fig. 1(d), becomes equivalent. This implies that the spin pairs on the diagonal bond J can be regarded as classical dimers.

References
[1] S. Yoshii, *et al.*, J. Phys.: Conf. Ser. **51**, 59 (2006).
[2] Z. Y. Meng and S. Wessel, Phys. Rev. B **79**, 104411 (2009).
[3] T. Suzuki, Y. Tomita, and N. Kawashima, Phys. Rev. B **80**, 180405(R) (2009).
[4] T. Suzuki, Y. Tomita, N. Kawashima, and P. Sengupta, Phys. Rev. B **82**, 214404 (2010).

Authors
T. Suzuki, Y. Tomita, P. Sengupta[a], and N. Kawashima
[a]Nanyang Technological University

Coarse-Grained Lipid Model for Large-Scale Simulations

Noguchi Group

Bilayer membranes exhibit many interesting phenomena such as shape deformation induced by phase separation or chemical reaction, membrane fusion, and membrane fission. Since the length scale of these phenomena widely varies from nano- to micro- meter scale, different types of membrane models are required to simulate each length scale. This year, we have developed a new coarse-grained molecular model to simulate bilayer membranes on a large length scale [1]. The solvent is implicitly represented by an effective attractive interaction between particles. A bilayer structure is formed by orientation-dependent (tilt and bending) potentials. In this model, the membrane properties (bending rigidity, line tension of membrane edge, area compression modulus, lateral diffusion coefficient, and flip-flop rate) can be varied over much wider ranges than in previous models. In particular, the bending rigidity and the line tension of membrane edge can be separately varied by changing different potential parameters.

Bilayer membranes and vesicles can be formed from a random gas state or a liquid droplet. Figure 1 shows an example of vesicle formation from the droplet. With a gradual increase in the strength of the tilt potential, which

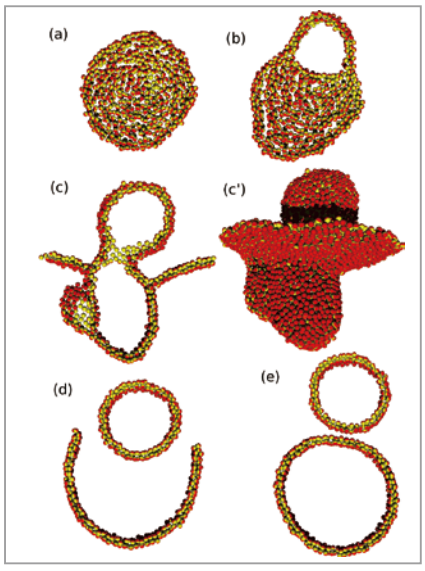

Fig. 1. Spontaneous formation of vesicles from a droplet. Sequential snapshots of (a)-(e) sliced and (c') entire membrane.

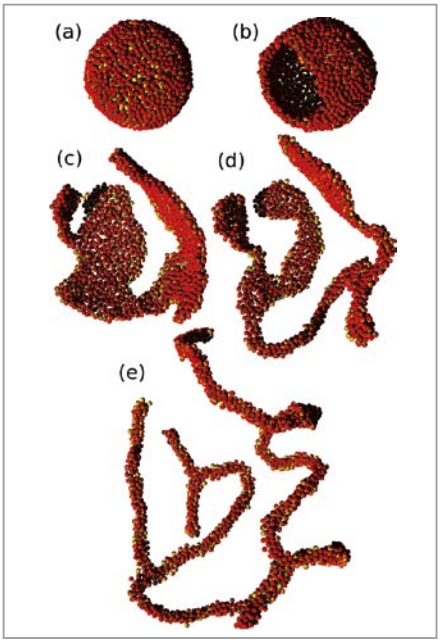

Fig. 2. Vesicle rupture to a work-like micelle.

represents the strength of amphiphilic interactions, a void space is opened in the droplet and results in the formation of two vesicles. If the separated membrane is small, a disk is formed instead of a veiscle. Since the larger droplets can have a clearer molecular layer on the surface, which prevents the shape change, the higher amphiphilicity is needed to trigger the shape transition. This droplet-bilayer transition can be used to investigate the stability of the bilayer structure.

Figure 2 shows the rupture of the membranes. The initial vesicle is metastable and maintains its shape for a short period. Then, a pore opens and grows to cracks. Finally, a branched worm-like micelle is formed. Here, we change the spontaneous curvature of the monolayer of the bilayer membrane. At large spontaneous curvature, a cylindrical structure becomes more favorable than the bilayer structure. This new model is suitable to study the molecular details of topological-change processes of the membrane, such as molecular self-assembly, pore formation, membrane fusion, and membrane fission. We plan to study the dynamics of the membrane fusion using this model.

Reference

[1] H. Noguchi, J. Chem. Phys. **134**, 055101 (2011).

Author
H. Noguchi

Upgrade of the Small-Angle Neutron Scattering Spectrometer SANS-U: a Focusing SANS Spectrometer

Shibayama Group

The SANS-U owned by the Institute for Solid State Physics, The University of Tokyo is one of conventional steady-state pinhole small-angle neutron scattering (PSANS) spectrometer operated in major research-reactor facilities in the world. First commissioned in 1991, the SANS-U was installed on the C1-2 cold neutron beam line at the research reactor (JRR-3) of the Japan Atomic Energy Agency (JAEA), Tokai, Japan. The total spectrometer length is 32 m. SANS-U has been upgraded several times [1,2] and various accessories, such as stretching device, high-pressure cell, and flow cell, are now available. As a result, the performance of SANS-U is now comparable to that of top-grade instruments in the world. On the other hand, chronic insufficiency of beam time became a crucial problem. Therefore, it was strongly desired to shorten the measurement time by increasing the neutron flux without loosing the spatial resolution. This problem was solved by introducing focusing small-angle neutron scattering (FSANS) coupled with a high-resolution area detector.

The upgrade of the SANS-U was undertaken to install a high-resolution position sensitive detector consisting of a cross-wired position sensitive photomultiplier tube combined with a ZnS/^{6}LiF scintillator on the SANS-U. By using both spherical MgF_2 biconcave lenses and the new high-resolution position sensitive detector, the accessible low Q-limit was extended from 2.5×10^{-3} to 3.8×10^{-4} Å^{-1}. As a result, the SANS-U can continuously cover a wide Q-range from 3.8×10^{-4} to 0.35 Å^{-1} with a wavelength of 7 Å. In order to confirm the reliability and the validity of the FSANS measurement, FSANS measurements were conducted on polystyrene (PS) latex with an average particle radius (R_{av}) of 2980 Å in H_2O. The sample-thickness of the latex dispersion was 1mm. Measurement times were 60 min for FSANS and 20 min for PSANS, respectively. Figure 1 shows the combined SANS profiles for the PS latex observed by the FSANS and the PSANS (L_2 = 8 and 1.03 m). The SANS profile obtained by the PSANS at L_2 = 12 m was also plotted for its vertical shift, being the best-resolution data obtained before the upgrade. In the PSANS profiles at higher Q-region of $Q > 1\times10^{-2}$ Å^{-1}, Q-independent scattering was observed, which was due to an incoherent scattering from H_2O. The Q_{min} was estimated to be 2.5×10^{-3} Å^{-1} for PSANS at L_2 = 12m and 3.8×10^{-4} Å^{-1} for the FSANS, respectively, indicating that the Q_{min} was successfully extended by about one order of magnitude. This result indicates that by

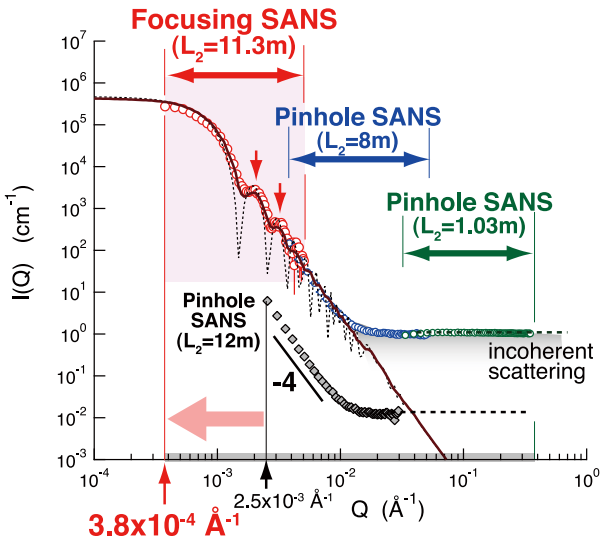

Fig. 1. Combined FSANS (red circles) and PSANS (L_2 = 8 m: blue circles and 1.03 m: green circles) profiles for polystyrene (PS) latex with an average particle radius of 2980 Å in H_2O. The PSANS profile (gray diamonds) obtained at L_2 = 12 m is vertically shifted to avoid overlaps, which is the highest-resolution data obtained before the upgrade. The dashed and solid lines are theoretical curve of the polydispersed sphere with the Schulz polydispersity distribution, simulated with catalog values; (solid line) the theoretical curve smeared by the instrumental resolution, (dashed line) the unsmeared curve.

employing FSANS (one condition) and conventional PSANS (two conditions; L_2 = 8 m and 1.03 m) with a wavelength of 7 Å, the SANS-U can continuously cover the wide Q-range from 3.8×10^{-4} to 0.35 Å^{-1} (approximately three orders of magnitude), which corresponds to a range of a few micrometers to several nanometers in real space. FSANS can be utilized not only to improve the accessible low Q-limit, but also to increase the incident-neutron flux in the conventional Q-range from 2.5×10^{-3} to 0.35 Å^{-1}. The "high-intensity" FSANS also allowed us to reduce measuring time by approximately 1/3.16 by increasing the incident neutron intensity.

References

[1] S. Okabe, M. Nagao, T. Karino, S. Watanabe, T. Adachi, H. Shimizu, and M. Shibayama, J. Appl. Cryst. **38**, 1035 (2005).
[2] S. Okabe, T. Karino, M. Nagao, S. Watanabe, and M. Shibayama, Nucl. Instrum. Methods A **572**, 853 (2007).
[3] H. Iwase, H. Endo, M. Katagiri, and M. Shibayama, J. Appl. Cryst. **44**, 558 (2011).

Authors

H. Iwase, H. Endo, M. Katagiri, and M. Shibayama

Spin Dynamics in Novel Rare-Earth Based Single-Molecule Magnets

Yamamuro Group

Single-molecule magnets (SMMs) are a class of metal-organic compounds in which each constituent molecule, containing magnetic atoms, possesses a giant and isolated resultant spin. When the giant spin exhibits easy-axis magnetic anisotropy (D<0), the molecule has a ground state

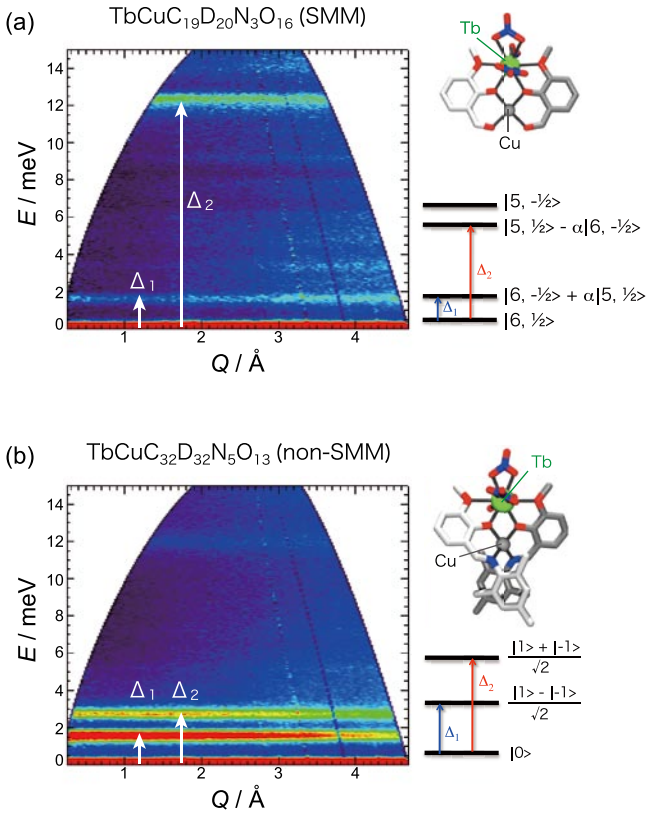

Fig. 1. Dynamical structure factors as functions of energy and momentum transfer for (a) complex 1 and (b) complex 2 taken at T = 6 K. Redder color denotes higher intensity. Molecular structures and energy scheme are also shown.

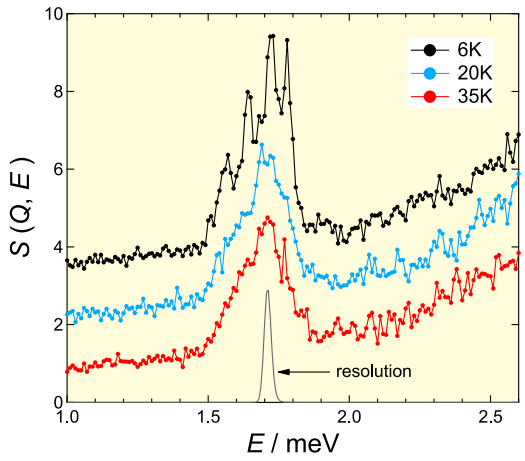

Fig. 2. Energy dependence of dynamical structure factors at T = 6, 20, and 35 K. Solid line represents the instrumental resolution.

with $S_z = \pm S$, and the potential barrier between the states can be simply described as DS_z^2. The presence of barrier yields a slow relaxation of the magnetization reversal that is characteristic of SMM. To date, SMMs containing transition metal atoms such as Mn, Fe, and Ni, have been intensively studied. Recently, a new series of rare-earth based SMMs was discovered and attracts much attention. Because of large contribution of angular momenta, lanthanide complexes can become SMMs containing only one or two magnetic atoms, being simpler than the transition metal SMMs consisting of many magnetic atoms and suitable for fundamental studies. Besides, the energy scale of lanthanide SMMs is expected to be larger and they can be good candidates for magnetic devices. Now we work on dinuclear SMMs consisting Tb^{3+} and Cu^{2+} ions. Interestingly, the system switches from SMMs to non-SMMs by a slight structural modification around the Tb^{3+} ions [1]. In order to investigate their spin states and energy scheme, we have performed inelastic neutron scattering experiments on the AMATERAS spectrometer newly built at J-PARC.

Figure 1 shows the dynamical structure factor, $S(Q,E)$, as functions of energy (E) and momentum transfer (Q) for $TbCuC_{19}D_{20}N_3O_{16}$ (complex 1 : SMM) and $TbCuC_{32}D_{32}N_5O_{13}$ (complex 2 : non-SMM). The $S(Q,E)$ map of complex 1 is much different from that of complex2. Taking account of scattering intensity and the selection rule, $\Delta S = \pm1$, we determined the energy scheme as shown in Fig. 1. In complex 1, the excitation with E = 1.7 meV corresponds to the transition from $|J_z=6, S_z=1/2\rangle$ to $|6, -1/2\rangle$, while that with E = 12.3 meV from $|6, 1/2\rangle$ to $|5, 1/2\rangle$, where J_z (S_z) is z-component of Tb^{3+} (Cu^{2+}) magnetic moment. Assuming the simple spin Hamiltonian, $H = DJ_z^2 + J_{ex}\,\boldsymbol{J}\cdot\boldsymbol{S}$, D and J_{ex} are estimated to be −1.1meV and −0.29 meV respectively. Note that the Tb^{3+} moment and the Cu^{2+} spin are coupled by the Heisenberg interaction. This is justified by the fact that the scattering intensity varies as $\sin(Qd)/Qd$, where d corresponds to the distance between Tb and Cu ions. It gives rise to the hybridization between $|6, -1/2\rangle$ and $|5, 1/2\rangle$ states.

On the other hand, for complex 2, it is the most plausible scheme that the ground state is $|J_z=0\rangle$ and the observed excitations around 2 meV corresponds to the excitations from $|J_z=0\rangle$ to $(|J_z=1\rangle\pm|J_z=-1\rangle)/\sqrt{2}$. Here, we neglect the contribution from the Cu^{2+} spin because the term, $\boldsymbol{J}\cdot\boldsymbol{S}$, must be small in this case. Assuming $H = DJ_z^2 + E(J_x^2 - J_y^2)$, we obtained D = 2.2 meV and E = 0.03 meV. Therefore, the magnetic anisotropy of Tb^{3+} in complex 1 (SMM) is

easy-axis type ($D < 0$), while that in complex 2 (non-SMM) easy-plane one ($D > 0$).

Now let us discuss the mechanism of magnetization reversal in complex 1. The activation energy estimated by the ac-magnetic susceptibility measurements is ca. 1.5meV [1] which is close to the energy difference between |6, 1/2> and |6, −1/2>. We speculate the magnetization reversal occurs through the quantum tunneling between |6, −1/2> and |−6, 1/2> states. However, the Hamiltonian mentioned above cannot cause the hybridization between these states. Our neutron scattering experiments under the high-resolution condition revealed that the peak at 1.7meV splits as shown in Fig. 2. This peak-splitting may result from the hyperfine interaction between the nuclear spin and electron spin and orbital magnetic moments. We predict that the hyperfine interaction plays an important role in the hybridization states that yield the tunneling process of magnetization reversal.

Reference

[1] T, Kajiwara, M. Nakano, S. Takaishi, and M. Yamashita, Inorg. Chem. **47**, 8604 (2008).

Authors

M. Kofu, O. Yamamuro, M. Nakano[a], and T. Kajiwara[b]

[a]Osaka University

[b]Nara Women's University

Pinwheel Valence-Bond-Solid in Quantum Kagome Antiferromagnet

Sato group

There has been a long-standing debate on the ground state of the quantum s = 1/2 kagome antiferromagnets. Theoretically, diverse classes of new states have been proposed, such as a gapless $U(1)$-Dirac-spin-liquid state, a gapped-spin-liquid state, and the valence-bond-solid (VBS) state, to note a few. As these quantum states lack static order, to distinguish them we need to investigate excited states, instead of the invisible non-magnetic ground state, using inelastic neutron scattering (INS).

There, however, has been a difficulty in investigating the quantum kagome antiferromagnets experimentally; no sizable single crystal has been available. Recently, researchers at Tokyo Tech discovered the stoichiometrically pure s = 1/2 deformed kagome antiferromagnet $Rb_2Cu_3SnF_{12}$, which can be grown in a large single crystal. This is the first realization of the INS-size quantum kagome crystal on the earth, and thus as soon as it was found we initiated extensive INS investigation to elucidate the nature of its non-trivial ground state [1].

The magnetic s = 1/2 Cu^{2+} ions reside at the corners of

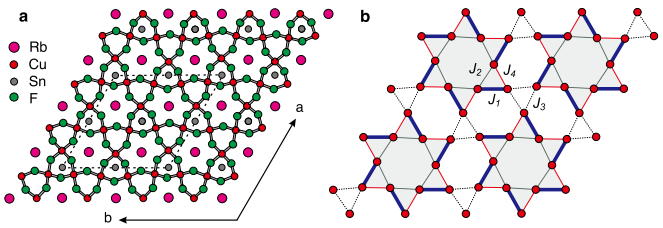

Fig. 1. (a) Crystal structure of $Rb_2Cu_3SnF_{12}$ in the hexagonal a-b plane. (b) The deformed kagome lattice of Cu^{2+} ions. Four different exchange paths are shown.

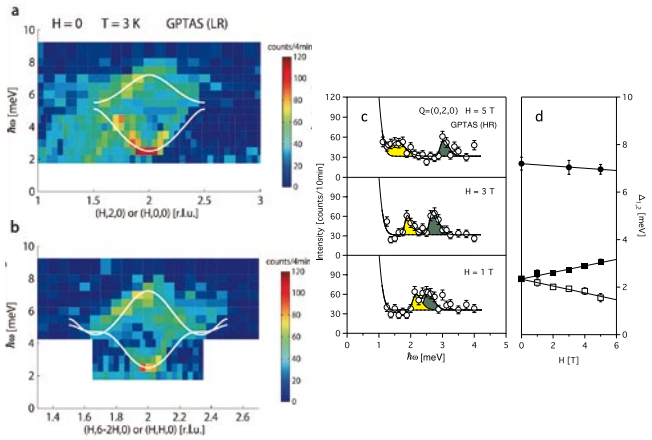

Fig. 2. (a, b) Inelastic scattering intensity map at the base temperature along the (a) $h00$ and (b) $hh0$ directions. (c) Inelastic scattering spectra at the Γ point under several external magnetic fields. (d) Magnetic field dependence of the excitation energies at the Γ point.

the triangles of the deformed single-layer kagome lattice (Fig. 1). The distortion yields four antiferromagnetic exchange interactions (J_1 to J_4). Crystallographically, the Dzyaloshinskii-Moriya (DM) interactions are also expected. Macroscopically, this system does not exhibit long-range order down to the lowest temperature; instead the magnetic susceptibility shows rapid decrease at low temperatures, indicating a formation of a singlet ground state.

Figure 2 shows the INS intensity maps along the $h00$ and $hh0$ directions. Clearly, two inelastic modes were observed; at the antiferromagnetic Γ point the lower energy branch can be found at $\hbar\omega \sim 2$ meV, whereas the higher at 7.5 meV. Prominent feature is their considerable dispersion in both the directions. The magnetic field dependence of the excitation energies at the Γ point is also given in Fig. 2. As seen in the figure, the lower-energy peak splits into two, indicating that they correspond to $S = 0$ to $S = 1$ ($S_z = \pm 1$) excitations, whereas the higher energy peak shows almost constant behavior, suggesting $S = 0$ to $S = 1$ ($S_z = 0$) excitation.

Assuming that the crystallographically short bond has the strongest antiferromagnetic interactions (i.e., J_1 is the strongest), singlet dimers may be formed on the J_1 bonds as a first approximation. This gives the pinwheel type spatial distribution of the singlet dimers as shown in Fig. 1. But are the other bonds are significantly weaker to localize the singlets to the J_1 bonds? We performed a detailed theoretical analysis using the dimer series expansion on the pinwheel VBS ground state. As a result, we found that all the four bonds are not so different, $J_2 = 0.95\ J_1$, $J_3 = 0.85\ J_1$ and $J_4 = 0.55\ J_1$, so the formation of the singlets only on the J_1 bonds is not trivial at all. In a theoretical study of the J_4-depleted kagome lattice, the pinwheel VBS state can be stabilized with J_4 only 3% smaller than J_1. The experimentally detected considerable dispersion of the triplet excitation modes is consistent with the almost equal interaction parameters, with which the excited triplets are not spatially localized, but move all around the deformed kagome lattice. Present result strongly suggests that the realization of the pinwheel VBS state in $Rb_2Cu_3SnF_{12}$ is not simply due to the crystallographic selection of single bond out of four, but due to the delicate imbalance of the geometrically frustrated antiferromagnetic interactions, highlighting the diversity and closeness of exotic phases in the quantum kagome lattice.

Reference

[1] K. Matan, T. Ono, Y. Fukumoto, T. J. Sato, J. Yamaura, M. Yano, K. Morita, and H. Tanaka, Nature Physics **6**, 865 (2010).

Authors
T. J. Sato, K. Matan[a], T. Ono[b], Y. Fukumoto[c], J. Yamaura, and H. Tanaka[d]
[a]Mahidol University
[b]Osaka Prefectural University
[c]Tokyo University of Science
[d]Tokyo Institute of Technology

Breakdown of Quasiparticle in Antiferromagnet

Masuda Group

Many phenomena in condensed matter science can be explained by using the concept of quasiparticle. For example antiferromagnetic order is a result of Bose condensation of magnons and superfluidity is those of phonons. The quasiparticle, however, can be unstable and decay if allowed by conservation laws. It was initially predicted in superfluid Helium and was identified by a termination of the excitation at twice the energy of a roton [1]. The magnon version of the spectral termination was observed in a few quantum magnets, where the one-magnon branch crosses the lower boundary of the two-magnon continuum. Recently the instability of magnons with a similar mechanism is predicted in the 2D square lattice Heisenberg antiferromagnets (SLHAF) in high magnetic field. At zero field a two-magnon continuum spreads in the higher energy region for all wave vector $\boldsymbol{q}$ and there is no decay channel. With increasing field the one-magnon branch moves to higher energy around $\boldsymbol{q}$ = (π, π) and eventually overlaps with the continuum at a threshold field. The hybridization of one-magnon with two-magnon continuum induces instability of the one-magnon. We report the experimental observation of the magnon instability in S=5/2 SLHAF $Ba_2MnGe_2O_7$ [2].

The susceptibility of $Ba_2MnGe_2O_7$ shows typical behavior of 2D SLHAF with J=0.026meV and T_N=4.0K. From magnetization measurement the saturation field is identified as low as 10T that enables systematic field effect study by combination of superconducting magnet and neutron scattering. Figure 1 shows magnetic excitation measured in various fields. With increasing field the energy of the main spin wave, mode 1, at $\boldsymbol{q}$ = (2 0 0) increases and the band energy reaches about 1.1 meV at H = 10 T (H_c).

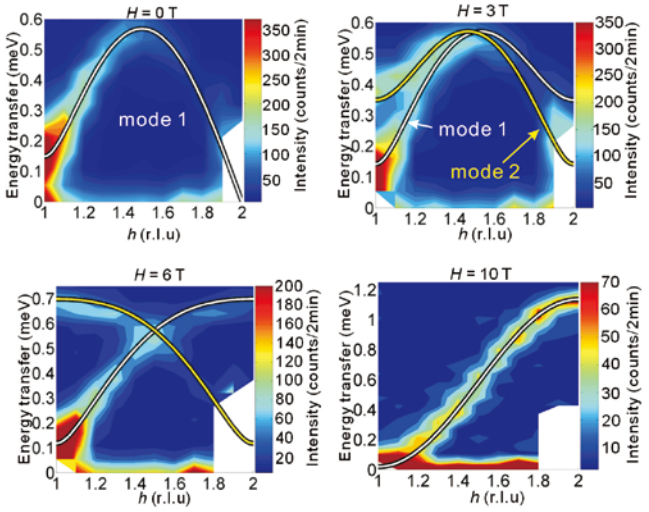

Fig. 1. Color plots of a series of constant q scans under magnetic fields. Solid curves are classical spin wave calculation.

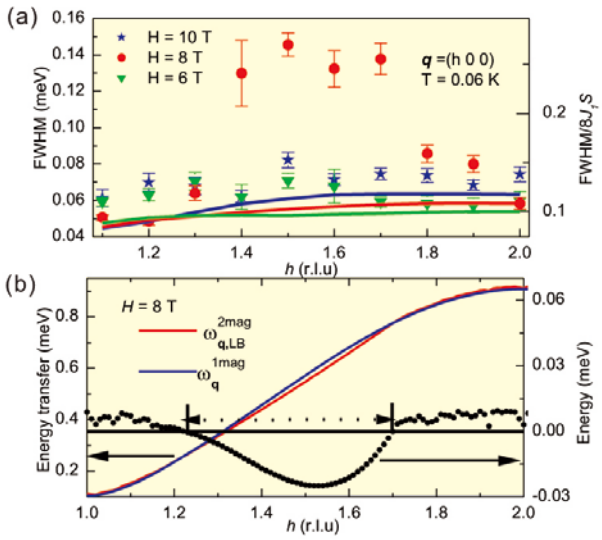

Fig.2 (a) Energy width of the constant q scans at different fields. Solid curves indicate the experimental resolution at the peak energies. (b) Blue curve is one-magnon energy and red curve is the lower boundary of calculated two magnon continuum. Symbols are the subtraction of the latter by the former. Dotted arrow indicates the decay channel allowed by conservation laws.

The dispersion has a ferromagnetic profile with reduced unit cell in the a plane at $H = H_C$. In the intermediate field another spin wave, mode 2, is induced due to doubling of the magnetic unit cell in the c direction. These excitations are qualitatively reproduced by spin wave calculation shown by solid curves. Figure 2(a) shows energy width of the magnetic excitation at $\boldsymbol{q}$ = (h 0 0). The broadening is clearly observed at 1.4 ≤ h ≤ 1.7 and H = 8T. This region is consistent with the numerically calculated magnon decay channel indicated by dotted arrow in Fig. 2(b). Hence the observed broadening of the peak profiles is ascribed to the field induced instability of magnon. A theoretical study is recently followed by a French group [3].

References
[1] E. Lifshits and L. Pitaevskii, *Statistical Physics II (Pergamon, Oxford, 1980).*
[2] T. Masuda *et al.*, Phys. Rev. B **81**, 100402 (2010).
[3] M. Mourigal *et al.*, Phys. Rev. B **82**, 144402 (2010).

Authors
T. Masuda, K. Kitaoka[a], S. Takamizawa[a], N. Metoki[b], K. Kaneko[b], K.C. Rule[c], K. Kiefer[c], H. Manaka[d], and H. Nojiri[e]
[a]Yokohama City University
[b]Japan Atomic Energy Agency
[c]Helmholtz Center Berlin
[d]Kagoshima University
[e]Tohoku University

Aharonov-Bohm Exciton Splitting in Chiral Specific Single-Walled Carbon Nanotubes Measured in Magnetic Fields of up to 78 T

Takeyama Group

A single-walled carbon nanotube (SWNT) is one of an ideal nanosystem for observation of the Aharanov-Bohm (AB) splitting of energy bands in an external magnetic field oriented parallel to the tube axis [1]. One dimensional properties of the SWNT induce pronounced 1D-exciton

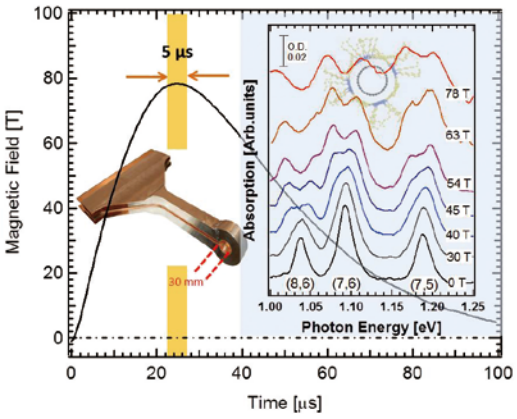

Fig. 1. The newly developed giant single-turn coil with a room temperature bore of 30 mm. The time signal profile of a magnetic field generated by the GSTC energized from the 5 MJ condenser bank system at ISSP, and the obtained magneto-optical near-infrared spectra at room temperature up to a magnetic field of 78 T applied to the PFO-SWNTs with (8,6), (7,6) and (7,5) chirality.

effects upon photoexcitation. Owing to the interplay between inter- and intra-K-K-valley short-range scattering, the exciton states are complicated with 16 split states of the bright and dark excitons. An external magnetic field causes the mixing of both states, and it is expected that the complicated exciton states can be clarified experimentally by application of a very high magnetic field. The observation of the exciton A-B splitting in various SWNTs has been reported by many authors so far by means of the absorption or by photoluminescence (PL) spectroscopy. The dark exciton states in ensemble samples have been reported in magneto-PL and in single SWNTs in micro-magneto-PL. However, there have never been quantitative analyses from magneto-absorption spectra owing to the enormous background absorption from the host solvent. The absorption measurement in a single SWNT is principally difficult. The PL in general is a process arising from a final state after an event of photo-excitation, and the coherency is therefore hindered by unknown impurities or localized states. Therefore it is important to observe the A-B coherent effect in magneto-absorption spectra for quantitative determination of the exciton states influenced purely by a magnetic field.

We could reduce contribution of the background absorption by employing PFO-SWNTs in which the polymer of 9, 9-dioctylfluorenyl-2,7-diyl referred as PFO was used as a solvent. The absorption spectra are well resolved owing to significant reduction of underlying background and also as a consequence of the high selectivity of the nanotube species of different chirality. Hence, magneto-optical absorption measurements on the chirality specific SWNTs at room temperatures were attempted to carried out at a near-infrared region up to a region of ultrahigh magnetic field.

The SWNT samples dispersed in a liquid solvent are kept in a glass cell, and measurements are to be carried out in a Voigt geometry ($\boldsymbol{k} \perp \boldsymbol{B}$), thus require a large sample space. Therefore, a new technology for magnetic field generation in room temperature large bore is required. In order to achieve this goal, the 'giant single-turn coil (GSTC) technique' is newly developed using a 5MJ condenser bank system conventionally used for the electro-magnetic flux compression at ISSP. The GSTC provides a peak magnetic field well above 100 T in a room temperature bore of 30 mm, and with time duration of almost 100 μs. The optical transmission signals of the near-infrared region were detected by InGaAs arrays with an exposure time of 5 μs synchronously opened the optical gate at the top of the pulse field.

Figure 1 shows the growth of splitting of the absorption peaks of (8,6), (7,6) and (7,5) chirality SWNT samples in magnetic fields up to 78 T. This is the world record data in a sense of application of such a high magnetic field to SWNTs with successful spectral resolution. Owing to a good resolution of the peak splitting, the precise dark-bright exciton splitting energies as well as the most reliable A-B exciton splitting parameters have been obtained, dependent on the tube diameter, for the first time. Quantitative comparison became possible to be carried out with existing theories [2].

References

[1] H. Ajiki and T. Ando, J. Phys. Soc. Jpn. **62**, 1255 (1993).
[2] S. Takeyama, H. Suzuki, H. Yokoi, Y. Murakami, and S. Maruyama, to be published in Phys. Rev. B (2011).

Authors
S. Takeyama, H. Suzuki, H. Yokoi[a], Y. Murakami[b], and S. Maruyama[c]
[a]Kumamoto University
[b]Tokyo Institute of Technology
[c]School of Engineering, The University of Tokyo

Measurement of Magneto-Caloric Effects in Pulsed-High Magnetic Fields

Tokunaga Group

Pulsed magnetic fields have been widely used to study various kinds of magnetic phase transitions in high magnetic fields. The measurable thermodynamic quantity in pulsed fields is, however, mostly limited to the magnetization. Measurements of the other quantity will provide novel possibility for the research of phase transitions in high magnetic fields. In this context, we are trying to develop a measurement system of magneto-caloric effects (MCEs) in pulsed magnetic fields.

Owing to the fast field-sweep ratio, pulsed fields are advantageous to magnetize the sample in the adiabatic condition. The most crucial technical point is how to measure the sample's temperature that changes momentary in pulsed fields. Our solution to this problem is the direct growth of resistive thermometers on top of the sample so as to minimize the heat capacity of the sensor and to maximize the thermal contact between the sensor and the sample. Putting this sample and thermometer in our adiabatic probe as illustrated in Fig. 1, we can measure MCEs in pulsed magnetic fields up to 55 T.

The results of the MCEs in polycrystalline gadolinium is shown in Fig. 2. As demonstrated in the inset, the measured

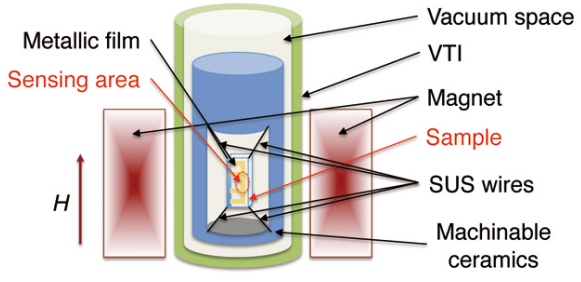

Fig. 1. Schematic illustration of the measurement system for the MCEs in pulsed magnetic fields. Resistive thermometers are grown directly on top of the sample. With measuring longitudinal magnetoresistance of the calibrated thermometer, we can evaluate the temperature change in the sample located in the center of the pulse magnet.

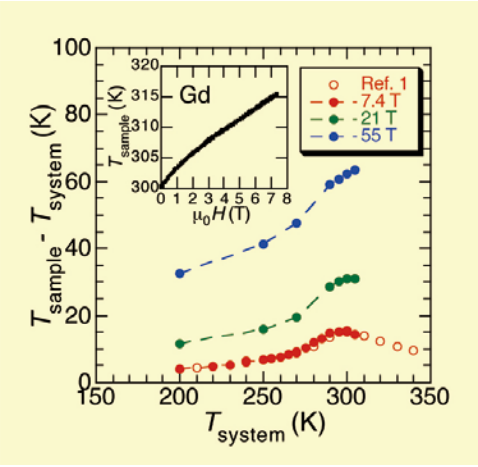

Fig. 2. Temperature change of polycrystalline gadolinium in adiabatic magnetization processes in pulsed fields (solid circles). The data at 7.4 T reasonably coincides with the reported data measured in steady fields (red open circles) [1]. (inset) The measured temperature of polycrystalline gadolinium (T_{sample}) as a function of applied fields.

temperature of the sample (T_{sample}) exhibits a monotonic trace as a function of magnetic field without showing any hysteresis between field-up and –down processes. The absence of the hysteresis guarantee the fast response of the thermometer with a time constant shorter than 0.1 ms. As shown in the main panel, the adiabatic temperature change (T_{sample} - T_{system}) measured in pulsed fields of 7.4 T (red solid circles) are reasonably coincide with those evaluated in steady fields (red open circles) [1]. In addition, our measurements in pulsed fields demonstrate the magneto-caloric heating over 60 K in applied fields of 55 T. Such direct evaluation of the MCEs in high fields will be effective to study the basic properties in materials useful for the magneto-caloric refrigeration at room temperature [2].

References
[1] V. K. Pecharsky and K. A. Gschneidner, Jr., Adv. Cryogen. Eng. **42A**, 423 (1996).
[2] E. Bruck, J. Phys. D: Appl. Phys. **38**, R381 (2005).

Authors
T. Kihara and M. Tokunaga

Magnetic-Field-Induced Valence Transition of $YbAgCu_4$ Observed by Synchrotron X-ray Absorption Spectroscopy

Y. Matsuda Group

Strong interaction between conduction electrons and f-electrons induces the heavy-fermion (HF) behavior in some rare-earth compounds containing Ce and Yb. The hybridization between the conduction and f electrons (c-f hybridization) is important to understand the exotic phenomena in the HF compounds. The occupation number of the f-shell is less than unity due to the c-f hybridization in a localized picture and the valence differs from the integer value. This is so called valence fluctuation phenomenon and observed in the HF compounds especially when the c-f hybridization is large and the Kondo temperature is high.

$YbAgCu_4$ shows HF behavior and valence fluctuation of the Yb at low temperatures. The electronic specific heat coefficient is 245 mJ/(mol K^2) and the Kondo temperature is

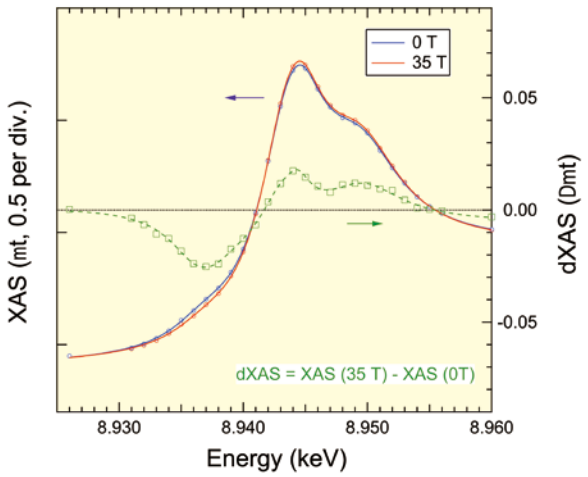

Fig. 1. X-ray absorption spectra (XAS) of $YbAgCu_4$ at 35 T and 0 T. The measurement temperature was 4.8 K. The difference spectrum (dXAS) obtained by the subtraction of 0 T spectrum from that of 35 T is shown by green open circles. The negative and positive structures in dXAS seen around 8.937 and 8.947 keV, respectively, indicate that the Yb valence increases toward trivalent state by applying a strong magnetic field.

about 200 K [1]. Recent theoretical work proposed that the unusual phenomena in the vicinity of the quantum critical point can occur due to the valence fluctuation [2]. According to the theory, $YbAgCu_4$ is located in the proximity of the critical end point of the valence transition and should show the valence change by applying a sufficient strong magnetic field. Since a microscopic measurement is required to observe the valence state, the magnetic field dependence of the Yb valence has never been clarified so far.

In this study, we have investigated the Yb valence states in high magnetic fields of up to 35 T using a pulsed magnet at SPring-8 BL39XU. Figure 1 shows the X-ray absorption spectra at near the L_3-edge of Yb at 0 and 35 T. The merit to measure the X-ray absorption is that the different valence states in rare-earth ions are observed as different absorption bands. The absorption band around 8.947 keV (double peak structure) is due to the Yb^{3+} state and that around 8.937 keV (shoulder structure) is due to the Yb^{2+} state. The difference spectrum between the absorption spectra at 35 T and 0 T is shown as the green open squares. Although the absorption change by magnetic field is as small as 1%, the difference spectrum clearly shows that the Yb^{3+} state enhances and the Yb^{2+} state diminishes by magnetic fields. This is a direct evidence of the magnetic field induced valence transition of this compound. The valence is deduced from the relative intensity of the absorption bands of both valence states. As

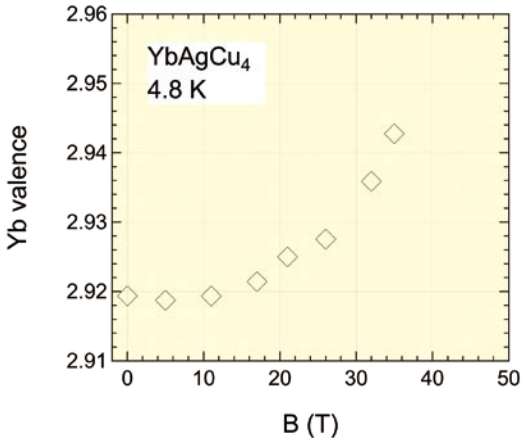

Fig. 2. Magnetic field dependence of the Yb valence in $YbAgCu_4$ at 4.8 K.

shown in Figure 2, the valence is insensitive to magnetic field at low fields up to around 10 T and increases with increasing magnetic fields. Since we also found that high magnetic field magnetization curve showed the small hysteresis, the observed magnetic-field-induced valence transition can be a first order transition.

References

[1] C. Rossel K. N. Yang, M. B. Maple, Z. Fisk, E. Zirngiebl, and J. D. Thompson, Phys. Rev. B **35**, 1914 (1987).
[2] S. Watanabe, A. Tsuruta, K. Miyake, and J. Flouquet, J. Phys. Soc. Jpn. **78**, 104706 (2010).

Authors

T. Nakamura, J. L. Her, Y. H. Matsuda, K. Kindo, T. Inami[a]. S. Michimura[a], M. Mizumaki[b], N. Kawamura[b], M. Suzuki[b], and K. Yoshimura[c]
[a]Japan Atomic Energy Agency
[b]Japan Synchrotron Radiation Research Institute / SPring-8
[c]Kyoto University